8-2011

Optimal Currents in Electrical Impedance Tomography with Robin Boundary Conditions

Cristoffer Cordes
Clemson University, cristoffer@cordes-hb.de

Optimal currents in electrical impedance tomography with Robin boundary conditions

---

A Master's Thesis
Presented to
the Graduate School of
Clemson University

In Partial Fulfillment
of the Requirements for the Degree
Master of Science
Mathematical Sciences

---

by
Cristoffer Cordes
August 2011

Accepted by:
Dr. Taufiquar Khan, Committee Chair
Dr. Jan Medlock
Dr. Jeong-Rock Yoon

Abstract

Electrical Impedance Tomography is an imaging technique with high potential in medical imaging. As of today the resolution is very low and measurement errors have a huge influence on the result.

In order to improve the results, the currents that are applied to perform the measurements have to be chosen carefully, and the best method to do so has not been found yet. For analytical and numerical convenience the spaces of the currents and voltages are often assumed to be $L_2(\partial\Omega)$. However, recent studies have shown that by introducing spaces that are more involved with the weak formulation of the problem, the algorithm of finding optimal currents gives significantly different results.
In addition the transition from posing the problem as a Neumann-to-Dirichlet experiment to posing it in a Robin-to-Dirichlet sense is often neglected due to the very similar nature of the resulting calculations.

This thesis investigates the impact of changing the boundary value problems in Electrical Impedance tomography from Neumann-to-Dirichlet to Robin-to-Dirichlet.
Several combinations of spaces for the Dirichlet and Robin data will be examined analytically and then compared to the according Neumann/Dirichlet spaces in a numerical simulation.

Acknowledgments

Foremost, I would like to express my gratitude to my advisor Dr. Taufiquar Khan for the support of my study and research, for his patience, guidance and enthusiasm.

Besides my advisor, I would like to thank the rest of my committee: Dr. Jan Medlock and Dr. Jeong-Rock Yoon for their encouragement.

I would also like to thank Prof. Dr. Peter Maaß and Dr. Ronald Stöver from Universität Bremen for giving me the opportunity to spend the past year in the graduate school of Clemson University.

Table of Contents

List of Tables

List of Figures

List of Symbols

Chapter 1

Introduction

1.1 Electrical Impedance Tomography

Electrical Impedance Tomography (EIT) is a relatively new imaging technique with applications in medicine and process control. The main idea is to obtain information about electrical properties of a region using measurements on the boundary of the region. EIT creates images of conductivity distributions, which are a measure of the resistance that a current experiences when it passes through a certain medium. There is a large contrast in conductivity between tissue, blood and air and even between normal and pathological tissue, therefore it is possible to use conductivity information to form anatomical images.

There are several reasons to prefer EIT over other medical imaging techniques such as X-ray CT - It is cheaper and faster, the required devices are much smaller and simpler and the procedure bears no risk for the patient's health. However, the resolution of the most recent devices are still far from comparable to MRT results.

One of the best examples for the advantage of EIT over the current diagnosis tools is the problem of finding blood clots in lungs. The present method involves inhaling radioactive gas to determine the ventilated lung region followed by an injection of radio-opaque dye into a vein to analyze the blood circulation. Finally, X-rays are used to calculate the image [1], whereas EIT only requires the application of electrodes on the patient's skin. Then a

current is generated and the voltage measurements are used to generate the image.

The first commercial EIT device for lung function monitoring was introduced in 2011. All other medical applications are still considered experimental. Other proposed applications include the detection of skin- and breast cancer and brain imaging, all of which have present diagnosis methods that involve ionizing radiation and expensive devices.

The biggest problem of reconstructing the conductivity in EIT is the ill-posed nature of the problem. The solution for a given set of EIT measurements exists and is unique, even when using a finite approximation, but it does not depend continuously on the data, meaning that for any given measurement precision there may be arbitrarily large changes in the conductivity distribution that are undetectable by the process. This difficulty can be controlled by including various physical restrictions to the mathematical problem that are known in advance. Another problem of this instability is the possibly huge influence of errors on the result, a small error can result in a very different picture, therefore the measurement process has to be chosen in a way that minimizes the influence of the errors.

One option to choose the currents that are used in order to extract information is to apply a deltoid or sinusoid current pattern at each combination of two of the electrodes and then using the resulting measurements to calculate the final image. The problem with this setup is that each current is weighted equally, thus a current that detects the conductivity fluctuation has the same influence on the final image as a current that only produces errors [1]. This leads one to choose the currents more carefully to improve the quality of the results.

1.2 Optimal currents

If we have a guess σ_0 for the actual conductivity σ_*, we want to know how good it is. Because we do not know the real conductivity in practical applications we have to introduce a criterion that does not use parameters that are not reachable by the physical

setup. One choice is the following:

$$\delta(j) = \frac{\|\varphi^*(j) - \varphi^0(j)\|}{\|j\|} \tag{1.1}$$

where φ^* is the result of the voltage measurement on the boundary and φ^0 is the result of a simulation of the voltage measurement using the conductivity σ_0. δ is called the distinguishability. If the distinguishability is close to zero, our simulation gives the same results for the voltage measurements as the physical setup for any chosen current, implying that the guess is good. However, this does not mean that our guess is accurate. Conductivity fluctuations at the center of the region are generally hard to detect by the setup of EIT, therefore the guess may be accurate near the boundary of the region but very rough at the center. The distinguishability only makes statements about the detectability of a difference between a guess and the actual physical conductivity. It is important for the technical setup of the problem that a distinguishability that is smaller than the noise ε does not lead to substantially different results.

Knowing the current that maximizes the distinguishability not only tells us how good our guess is, it also tells us how to choose a current to make the inaccuracies of the guess visible. From a theoretical point of view any full linearly independent set of currents will extract all possible information from the system since the problem is very close to being linear [1]. However, if we know which currents are able to extract the most information we can weigh those currents to steer against the measurement errors of the less important ones and significantly improve the final result.

In order to find the optimal currents one has to assume that the current patterns are in a certain function space, i.e. possess a certain smoothness. Recent results show that the setting $L_2(\partial\Omega) \to L_2(\partial\Omega)$ which is often chosen for numerical convenience can be significantly improved by introducing spaces that are more involved with the setup of the problem. Another simplification is the assumption of the currents being boundary data to a PDE with Neumann boundary conditions rather than Robin boundary conditions. The

influence of this change in boundary data will be examined in this thesis while taking various function spaces into account.

The next chapter will introduce the problem in a mathematical way and derive the Hilbert spaces that are needed to perform most of the calculations of this thesis. It will do so in Neumann-to-Dirichlet and Robin-to-Dirichlet sense to emphasize the similarities. The second chapter will also explain the Power Method, which is the main tool used for the numerical simulations.

Chapter 3 is the analytical part of this thesis. It will find the adjoint operators that the Power Method needs in order to find the optimal currents.

Chapter 4 introduces the MATLAB algorithm that is used for the simulations and gives results which are then discussed in the last chapter.

Chapter 2

Problem

For $\Omega \subset \mathbb{R}^n (n = 2, 3)$ with a smooth boundary $\partial\Omega$, we assume that the conductivity σ is a distribution that is bounded above and below and strictly positive. It is also assumed that there are no current sources inside of Ω. Therefore, using the Maxwell-equations, the distribution of the electric potential inside of Ω is a solution of the following elliptic equation:

$$-div(\sigma \nabla u) = 0 \quad \text{in } \Omega. \tag{2.1}$$

An EIT experiment then consists of applying an electrical current (Neumann data) j on the boundary $\partial\Omega$ followed by measuring the potential φ on $\partial\Omega$ (Dirichlet data). This results in information about the Neumann-to-Dirichlet (NtD) map which is then ultimately used to reconstruct σ.

2.1 Neumann-to-Dirichlet setting

For the Neumann-to-Dirichlet setting the boundary value problems that describe the EIT measurements are defined as follows:

The Neumann problem is

$$\begin{aligned} -div(\sigma \nabla u) &= 0 \quad \text{in } \Omega \\ \sigma \frac{\partial u}{\partial n} &= j \quad \text{on } \partial\Omega \end{aligned} \tag{2.2}$$

and the Dirichlet problem is given by

$$\begin{aligned} -div(\sigma \nabla u) &= 0 \quad \text{in } \Omega \\ \sigma u &= \varphi \quad \text{on } \partial\Omega. \end{aligned} \tag{2.3}$$

Where σ is bounded above and below, say $\varepsilon < \sigma < \frac{1}{\varepsilon}$ and $\Omega \subset \mathbb{R}^2$. Let Z denote the space of functions defined on the boundary for the Dirichlet setting, let X denote the space of functions defined on the boundary for the Neumann boundary value problem, and finally let Y be the space on which the solutions u are defined.

Let γ_D denote the Dirichlet trace - the restriction of u to the boundary:

$$\gamma_D : \quad Y \to Z \tag{2.4}$$

$$u \mapsto u|_{\partial\Omega} \tag{2.5}$$

The operator $\sigma \frac{\partial}{\partial n}$ is called the Neumann trace:

$$\sigma \frac{\partial}{\partial n} : \quad Y \to X \tag{2.6}$$

$$u \mapsto \sigma \frac{\partial}{\partial n} u. \tag{2.7}$$

For the NtD-setting in EIT we need

$$\int_{\partial\Omega} \gamma_D u(s) ds = 0 \tag{2.8}$$

to ensure the uniqueness of the solution. Also the Neumann problem only has a solution if the current satisfies the integrability condition, thus

$$\int_{\partial\Omega} j(s)ds = 0 \tag{2.9}$$

has to be enforced as well.[2]

Then, since each problem has a unique solution, we can define the extension operators for the two problems as follows.

$$F_N^\sigma : \quad X \to Y \tag{2.10}$$

$$j \mapsto u \quad \text{u solves (2.2)} \tag{2.11}$$

and

$$F_D^\sigma : \quad Z \to Y \tag{2.12}$$

$$\varphi \mapsto u \quad \text{u solves (2.3).} \tag{2.13}$$

Using this notation and the weak formulation of the Neumann problem we get:

$$0 = -\int_\Omega div(\nabla\sigma u)\cdot v dx \tag{2.14}$$

$$= -\int_{\partial\Omega} j\gamma_D v ds + \int_\Omega \sigma\nabla F_N^\sigma(j)\cdot\nabla v dx. \tag{2.15}$$

So:

$$\int_{\partial\Omega} j\gamma_D v ds = \int_\Omega \sigma\nabla F_N^\sigma(j)\cdot\nabla v dx. \tag{2.16}$$

Depending on the choice of X, Y and Z, the boundary integral should be understood as a corresponding duality pairing.

There are several choices for the spaces X, Y and Z. For convenience, the most

commonly used combination for the NtD mapping is $X = L_2(\partial\Omega), Y = H^1(\Omega), Z = L_2(\partial\Omega)$. However, the choice of the spaces heavily influences the results for the optimal currents, therefore it is of use to also examine the following spaces.

For the solution space:

$$Y = \tilde{H}^1_\sigma(\Omega) = \left\{ u \in L_2(\Omega) | \int_\Omega \sigma(x) |\nabla u(x)|^2 dx < \infty, \int_{\partial\Omega} \gamma_D u(s) ds = 0 \right\}. \tag{2.17}$$

This turns out to be a good choice for analytical matters because the inducing inner product

$$\langle u, v \rangle_{\tilde{H}^1_\sigma} = \int_\Omega \sigma \nabla u \cdot \nabla v dx \tag{2.18}$$

is directly correlated with the weak formulation of the problem. Note that (2.8) is necessary to make the bilinear form an inner product. This inner product can now be used to define spaces and inner products for the boundary distributions using the extension operator

$$Z = \tilde{H}^{1/2}_\sigma(\partial\Omega) = \left\{ g \in L_2(\partial\Omega) | \int_\Omega \sigma(x) |\nabla F^\sigma_D g(x)|^2 dx < \infty, \int_{\partial\Omega} g(s) ds = 0 \right\}, \tag{2.19}$$

and the corresponding inner product

$$\langle g, h \rangle_{\tilde{H}^{1/2}_\sigma} = \int_\Omega \sigma \nabla F^\sigma_D g \cdot \nabla F^\sigma_D h dx. \tag{2.20}$$

The easiest way to introduce the suitable space for the Neumann boundary is to make use of the fact that the Dirichlet-to-Neumann operator $\sigma \frac{\partial}{\partial n} F^\sigma_D$ is well defined on $\tilde{H}^{1/2}_\sigma$, so:

$$X = \tilde{H}^{-1/2}_\sigma(\partial\Omega) = \left\{ f | f = \sigma \frac{\partial}{\partial n} F^\sigma_D g, g \in \tilde{H}^{1/2}_\sigma \right\}, \tag{2.21}$$

which makes X the dual space of Y. And again the extension operator leads to the natural choice for an inner product on this space:

$$\langle f, h \rangle_{\tilde{H}^{-1/2}_\sigma} = \int_\Omega \sigma \nabla F^\sigma_N f \cdot \nabla F^\sigma_N h dx. \tag{2.22}$$

2.2 Robin-to-Dirichlet setting

The main emphasis of this thesis is to analyze the impact of using a mixed (Robin) boundary condition instead of the Neumann boundary condition. Thus we are interested in the analytical and numerical properties of the Robin-to-Dirichlet map and aim at comparing the resulting distinguishability criteria. The new boundary value problems are as follows:

Robin Problem:

$$\begin{aligned} -div(\sigma \nabla u) &= 0 \quad \text{in } \Omega \\ \sigma \frac{\partial u}{\partial n} + \alpha \gamma_D u &= j \quad \text{on } \partial\Omega. \end{aligned} \tag{2.23}$$

The Dirichlet problem stays the same:

$$\begin{aligned} -div(\sigma \nabla u) &= 0 \quad \text{in } \Omega \\ u &= \varphi \quad \text{on } \partial\Omega. \end{aligned} \tag{2.24}$$

We do not need to enforce $\int_{\partial\Omega} \gamma_D u(s) ds = 0$ to gain uniqueness of the solution of the Robin problem which is a main difference between the Robin problem and the Neumann problem. Furthermore it is no longer necessary to require $\int_{\partial\Omega} j(s) ds = 0$ since the Robin problem always has a solution.

Analogously to the NtD setting we introduce the linear forward operator of the Robin problem

$$F_R^\sigma : \quad X \to Y \tag{2.25}$$

$$j \mapsto u \quad \text{u solves (2.23).} \tag{2.26}$$

Now use the weak formulation of the Robin boundary value problem

$$0 = -\int_\Omega div(\sigma \nabla u) \cdot v dx \tag{2.27}$$

$$= -\int_{\partial\Omega} \sigma \frac{\partial}{\partial n} u \cdot \gamma_D v ds + \int_\Omega \nabla u \cdot \nabla v dx \tag{2.28}$$

$$= -\int_{\partial\Omega} j \cdot \gamma_D v ds + \alpha \int_{\partial\Omega} u\gamma_D \cdot v ds + \int_\Omega \nabla u \cdot \nabla v dx \tag{2.29}$$

which leads us to the equality:

$$\int_\Omega \sigma \nabla u \cdot \nabla v dx + \alpha \int_{\partial\Omega} \gamma_D u \cdot \gamma_D v ds = \int_{\partial\Omega} f \gamma_D v ds. \tag{2.30}$$

Using this formula as a starting point, we obtain a solution space with good properties:

$$Y = H^1_\sigma = \left\{ u \in L_2(\Omega) | \int_\Omega \sigma(x) |\nabla u(x)|^2 dx + \alpha \int_{\partial\Omega} |\gamma_D u(x)|^2 ds < \infty \right\}, \tag{2.31}$$

because it suggests the inner product:

$$\langle u, v \rangle_{H^1_\sigma} = \int_\Omega \sigma(x) \nabla u(x) \cdot \nabla v(x) dx + \alpha \int_{\partial\Omega} \gamma_D u(x) \cdot \gamma_D v(x) ds. \tag{2.32}$$

Note that, opposed to the NtD setting, constant distributions do not result in the norm being zero, so we do not need the vanishing boundary integral that we had to enforce in (2.8). [5]

Now we can continue as we did before and define Z using the extension operator:

$$Z = H^{1/2}_\sigma = \left\{ g \in L_2(\partial\Omega) | < F^\sigma_D g, F^\sigma_D g >_{H^1_\sigma} < \infty \right\} \tag{2.33}$$

$$= \left\{ g \in L_2(\partial\Omega) | \int_\Omega \sigma(x) |\nabla F^\sigma_D g|^2 dx + \alpha \int_{\partial\Omega} |\gamma_D F^\sigma_D g|^2 ds < \infty \right\}. \tag{2.34}$$

And we can use the inner product of Y to define an inner product on Z:

$$\langle g, h \rangle_{H^{1/2}_\sigma} = \int_\Omega \sigma \nabla F^\sigma_D g \cdot \nabla F^\sigma_D h dx + \alpha \int_{\partial\Omega} \gamma_D F^\sigma_D g \cdot \gamma_D F^\sigma_D h ds. \tag{2.35}$$

Again, the easiest way to construct the suitable space for the Robin boundary distributions is to define it as the dual of Z:

$$X = H_\sigma^{-1/2}(\partial\Omega) = \left\{ f | f = \left(\sigma \frac{\partial}{\partial n} + \alpha\gamma_D \right) F_D^\sigma g, g \in H_\sigma^{1/2} \right\}. \tag{2.36}$$

The resulting space is then equipped with the inner product:

$$\langle f, g \rangle_{H_\sigma^{-1/2}} = \int_\Omega \sigma \nabla F_R^\sigma f \cdot \nabla F_R^\sigma g dx + \alpha \int_{\partial\Omega} \gamma_D F_R^\sigma f \cdot \gamma_D F_R^\sigma g ds. \tag{2.37}$$

2.3 Calculating optimal currents

As mentioned before, the goal is to construct optimal input currents. We want to find current patterns j allowing us to best distinguish between our guess σ_0 and the real conductivity σ_*, so from a theoretical point of view we want to find

$$\max_{j, \|j\|_X = 1} \|\varphi^* - \varphi^0\|_Z. \tag{2.38}$$

A very practical tool to find this optimal current is the Power Method.
But first recall the definition of the adjoint operator:

Definition 1. *For a continuous linear operator $A : H_1 \to H_2$ between two Hilbert spaces, there exists a unique continuous linear operator $A^* : H_2 \to H_1$ with the property:*

$$\langle Ax, y \rangle = \langle x, A^* y \rangle \quad \textit{for all } x \in H_1, y \in H_2. \tag{2.39}$$

A^* is called the adjoint of A.

With the help of the adjoint operator it is then possible to find the norm of a NtD or RtD distinguishability operator A in a different way:

$$\max_{j,\|j\|_X=1} \|\varphi^*(j) - \varphi^0(j)\|_Z = \max_{j,\|j\|_X=1} \|A(j)\|_Z \tag{2.40}$$

$$= \max_{j,j\neq 0} \frac{\|A(j)\|_Z}{\|j\|_X} \tag{2.41}$$

$$= \|A\|_{X\to Z}. \tag{2.42}$$

Let $\mathcal{A} : X \to X$ be given by $\mathcal{A} = A^*A$. Then:

$$\|A\|^2_{X\to Z} = \sup_{j,j\neq 0} \frac{\langle Aj, Aj\rangle_Z}{\langle j, j\rangle_X} \tag{2.43}$$

$$= \sup_{j,j\neq 0} \frac{\langle A^*Aj, j\rangle_X}{\langle j, j\rangle_X} \tag{2.44}$$

$$= \sup_{j,j\neq 0} \frac{\langle \mathcal{A}j, j\rangle_X}{\langle j, j\rangle_X}. \tag{2.45}$$

For a compact, self-adjoint and non-negative $\mathcal{A}$, the spectrum consists of a discrete set $\lambda_n \to 0$ and we can form an orthonormal basis consisting of corresponding eigenfunctions. By applying the Minimax Principle, it follows that the optimal currents are to be chosen as the eigenfunctions with the largest eigenvalues.

Theorem 1. *The source j_{sup} that maximizes the distinguishability is an eigenfunction corresponding to the largest eigenvalue λ_1.*
Furthermore, for any $j \in X$ with $\langle j_{sup}, j\rangle \neq 0$:

$$\lim_{n\to\infty} \frac{\mathcal{A}^n j}{\|\mathcal{A}^n j\|_X} = j_{sup} \tag{2.46}$$

Note that $\|A\|_{X\to Z} = \sqrt{\lambda_1}$.

Proof. The first part follows directly from the Minimax Principle as mentioned above. For the second part: Express j as a linear combination of the orthonormal basis $\{\phi_k\}_{k\in\mathbb{N}}$ of $\mathcal{A}$'s

eigenvectors:

$$j = \sum_{k=1}^{\infty} < j, \phi_k >_X \phi_k. \tag{2.47}$$

Since all ϕ_k are eigenfunctions, we get:

$$\mathcal{A}^n j = \sum_{k=1}^{\infty} \langle j, \phi_k \rangle (\lambda_k)^n \phi_k \tag{2.48}$$

$$= \langle j, \phi_1 \rangle (\lambda_1)^n \phi_1 + \sum_{k=2}^{\infty} \langle j, \phi_k \rangle (\lambda_k)^n \phi_k \tag{2.49}$$

$$= (\lambda_1)^n (\langle j, \phi_1 \rangle \phi_1 + \sum_{k=2}^{\infty} \langle j, \phi_k \rangle (\frac{\lambda_k}{\lambda_1})^n \phi_k), \tag{2.50}$$

and taking the norm yields:

$$\|\mathcal{A}^n j\|_X = (\lambda_1)^n |\langle j, \phi_1 \rangle| \sqrt{1 + \sum_{k=2}^{\infty} (\frac{\langle j, \phi_k \rangle \lambda_k}{\langle j, \phi_1 \rangle \lambda_1})^{2n} \phi_k}. \tag{2.51}$$

Since λ_1 is the biggest eigenvalue, the infinite sums decay to zero exponentially fast. Taking the limit results in:

$$\lim_{n \to \infty} \frac{\mathcal{A}^n j}{\|\mathcal{A}^n j\|} = \frac{\langle j, \phi_1 \rangle \phi_1}{|\langle j, \phi_1 \rangle|} = \pm \phi_1 = j_{sup}. \tag{2.52}$$

□

Note that an eigenvector with the second largest eigenvalue can be obtained by introducing a new operator $\mathcal{A}_2 = \mathcal{A} - \langle \phi_1, \cdot \rangle \phi_1$ and applying the Power Method once more.

Chapter 3

Adjoint calculations

Since the Power Method is the heart of the algorithm for determining optimal currents, the adjoint calculations are the major part of the theory behind it.

Each choice of spaces is involved with embedding operators that have nontrivial adjoints, so every space setting has to be discussed separately. However, it is a good idea to first calculate the adjoints of the reappearing operators and put them together afterwards to construct the adjoints of the distinguishability criteria.

3.1 Distinguishability criteria

There are two choices for the Dirichlet space and two choices for the Robin space giving us a total of four combinations and therefore the following four distinguishability criteria:

$$A_1 : L_2 \to L_2 : \qquad j \mapsto \gamma_D F_R^{\sigma_0}(j) - \gamma_D F_R^{\sigma_*}(j) \tag{3.1}$$

$$A_2 : H_{\sigma_0}^{-1/2} \to H_{\sigma_0}^{1/2} : \qquad j \mapsto \gamma_D F_R^{\sigma_0}(j) - i_+ \gamma_D F_R^{\sigma_*} i_-(j) \tag{3.2}$$

$$A_3 : L_2 \to H_{\sigma_0}^{1/2} : \qquad j \mapsto \gamma_D F_R^{\sigma_0} I_-^{\sigma_0}(j) - i_+ \gamma_D F_R^{\sigma_*} i_- I_-^{\sigma_0}(j) \tag{3.3}$$

$$A_4 : H_{\sigma_0}^{-1/2} \to L_2 : \qquad j \mapsto I_+^{\sigma_0} \gamma_D F_R^{\sigma_0}(j) - I_+^{\sigma_0} i_+ \gamma_D F_R^{\sigma_*} i_-(j). \tag{3.4}$$

The i and I operators are embeddings. They will be introduced properly later. The following paragraph will briefly outline why embeddings are necessary:

A_1 goes from L_2 to L_2, so there are no embedding operators necessary.

A_2 goes from $H_{\sigma_0}^{-1/2}$ to $H_{\sigma_0}^{1/2}$ but it also involves the Robin extension going from $H_{\sigma_*}^{-1/2}$ to $H_{\sigma_*}^{1}$, so an embedding going from $H_{\sigma_0}^{-1/2}$ to $H_{\sigma_*}^{-1/2}$ is needed before applying the extension. And afterwards we need another inclusion to get from $H_{\sigma_*}^{1/2}$ to $H_{\sigma_0}^{1/2}$.

For the mixed case A_3 we start off at the smoother space L_2 but want to end up in $H_{\sigma_0}^{1/2}$ and therefore need to apply the RtD map having $H_{\sigma_0}^{-1/2}$ as the domain. So we need the embedding $L_2 \hookrightarrow H_{\sigma_0}^{-1/2}$ before applying the extension.

Similarly, for A_4, after applying the extension operator we end up in $H_{\sigma_0}^{1/2}$ but are required to end up in L_2, so we need the embedding $H_{\sigma_0}^{1/2} \hookrightarrow L_2$.

3.2 Identities

The knowledge of some identities is necessary to perform the adjoint calculations:

Lemma 1. *The following identities hold.*

$$\gamma_D F_D^\sigma = id_D \tag{3.5}$$

$$\left(\sigma\frac{\partial}{\partial n} + \alpha\gamma_D\right) F_R^\sigma = id_R \tag{3.6}$$

$$F_R^\sigma \left(\sigma\frac{\partial}{\partial n} + \alpha\gamma_D\right) F_D^\sigma = F_D^\sigma \tag{3.7}$$

$$F_D^\sigma(\gamma_D F_R^\sigma) = F_R^\sigma \tag{3.8}$$

$$\left(\sigma\frac{\partial}{\partial n} + \alpha\gamma_D\right) F_D^\sigma \gamma_D F_R^\sigma = id_R \tag{3.9}$$

$$\gamma_D F_R^\sigma \left(\sigma\frac{\partial}{\partial n} + \alpha\gamma_D\right) F_D^\sigma = id_D. \tag{3.10}$$

Proof. To understand these identities, it is important to keep in mind that the extension operators and traces are connecting the boundary distributions and the unique solutions to the problem.

In other words: If we start with a solution $u \in Y$ to both problems, taking either trace followed by the corresponding extension operator will map back to the same u, and since the RtD map is bijective, starting in either boundary space and applying the extension operator will result in a solution u to both boundary value problems.
The above mentioned identities express this idea in various ways:

- (3.5) follows directly from the definition of the Dirichlet extension.
- (3.6) is also a direct consequence from the definition of the corresponding extension operator.
- (3.7) holds because after solving the Dirichlet problem with boundary distribution $\varphi \in Z$ and obtaining the solution $u \in Y$, we know that the Robin trace $j \in X$ of u has a unique solution to the Robin boundary value problem. Since it is the Robin trace of u, u must be that solution and therefore F_R^σ maps j to u giving us the identity.
- (3.8) is true because of the same argument by switching the roles of Z and X.
- (3.9) can be explained as follows: For a Robin boundary distribution $j \in X$ we apply the extension operator. The solution $u \in Y$ is not changed by taking the Dirichlet trace followed by the Dirichlet extension. Applying the Robin trace afterwards leads back to the initial distribution j.
- (3.10) again can be obtained by switching the roles of the spaces X and Z of the previous identity.

□

3.3 Fundamental adjoints

In order to calculate the adjoints of the distinguishability criteria, it is useful to know the adjoints of their building blocks. This section is going to deal with the calculations of those fundamental adjoints.

Lemma 2. *The adjoints that are needed to assemble the adjoints of the distinguishability criteria are given by:*

$$\gamma_D F_R^\sigma : \quad L_2 \to L_2 \qquad (\gamma_D F_R^\sigma)^* = \gamma_D F_R^\sigma \tag{3.11}$$

$$\gamma_D F_R^\sigma : \quad H_\sigma^{-1/2} \to H_\sigma^{1/2} \qquad (\gamma_D F_R^\sigma)^* = \left(\sigma \frac{\partial}{\partial n} + \alpha \gamma_D\right) F_D^\sigma \tag{3.12}$$

$$i_+ : \quad H_{\sigma_*}^{1/2} \hookrightarrow H_{\sigma_0}^{1/2} \qquad (i_+)^* = \gamma_D F_R^{\sigma_*} \left(\sigma_0 \frac{\partial}{\partial n} + \alpha \gamma_D\right) F_D^{\sigma_0} \tag{3.13}$$

$$i_- : \quad H_{\sigma_0}^{-1/2} \hookrightarrow H_{\sigma_*}^{-1/2} \qquad (i_-)^* = \left(\sigma_0 \frac{\partial}{\partial n} + \alpha \gamma_D\right) F_D^{\sigma_0} \gamma_D F_R^{\sigma_*} \tag{3.14}$$

$$I_-^\sigma : \quad L_2 \hookrightarrow H_\sigma^{-1/2} \qquad (I_-^\sigma)^* = \gamma_D F_R^\sigma \tag{3.15}$$

$$I_+^\sigma : \quad H_\sigma^{1/2} \hookrightarrow L_2 \qquad (I_+^\sigma)^* = \gamma_D F_R^\sigma. \tag{3.16}$$

Proof. The general technique to determine the adjoint operators is to evaluate both sides of the defining equality of the adjoint operator and then comparing them after manipulating both sides.

3.3.1 $A : L_2 \to L_2 : \quad j \mapsto \gamma_D F_R^\sigma j$

We start with writing out the definition of the inner product.

$$
\begin{aligned}
< Af, g >_{L_2} &= \int_{\partial\Omega} \gamma_D F_R^\sigma(f) \cdot g ds && (3.17)\\
&= \int_\Omega \sigma \nabla F_D^\sigma \gamma_D F_R^\sigma(f) \cdot \nabla F_R^\sigma(g) dx + \alpha \int_{\partial\Omega} \gamma_D F_R^\sigma(f) \cdot \gamma_D F_R^\sigma g ds && (3.18)\\
&= \int_{\partial\Omega} \sigma \frac{\partial}{\partial n} F_D^\sigma \gamma_D F_R^\sigma(f) \cdot \gamma_D F_R^\sigma(g) ds + \alpha \int_{\partial\Omega} \gamma_D F_R^\sigma(f) \cdot \gamma_D F_R^\sigma(g) ds && (3.19)\\
&= \int_{\partial\Omega} (\sigma \frac{\partial}{\partial n} F_D^\sigma \gamma_D F_R^\sigma(f) + \alpha \gamma_D F_R^\sigma(f)) \cdot \gamma_D F_R^\sigma(g) ds && (3.20)\\
&= \int_{\partial\Omega} (\left(\sigma \frac{\partial}{\partial n} + \alpha \gamma_D \right) F_R^\sigma(f)) \cdot \gamma_D F_R^\sigma(g) ds && (3.21)\\
&= \int_{\partial\Omega} f \cdot \gamma_D F_R^\sigma(g) ds && (3.22)\\
&= \int_{\partial\Omega} f \cdot A g ds && (3.23)\\
&=< f, Ag >_{L_2} . && (3.24)
\end{aligned}
$$

For (3.18) we make use of the weak formulation (2.30) of the Robin problem. In (3.19) we use partial integration. Note that $div(\sigma \nabla u) = 0$, so the domain-integral vanishes. Now that the integrals are both defined on the boundary, they can be combined in (3.20); they can be put together this way because all operators are linear. This can be written in a slightly better way (3.21) using the identity (3.8). Now we use (3.6) to get to (3.22) and end up with an expression that agrees with the defining property of the adjoint operator, thus implying that A is self-adjoint.

3.3.2 $A : H_\sigma^{-1/2} \to H_\sigma^{1/2} : \quad j \mapsto \gamma_D F_R^\sigma j$

Even though the operator is numerically the same as before, the adjoint turns out to be very different. We start by evaluating the inner product on the Dirichlet side:

$$< Af, g >_{H_\sigma^{1/2}} = \int_\Omega \sigma \nabla F_D^\sigma \gamma_D F_R^\sigma(f) \cdot \nabla F_D^\sigma(g) dx + \alpha \int_{\partial\Omega} \gamma_D F_R^\sigma(f) \cdot \gamma_D F_D^\sigma g ds \tag{3.25}$$

$$= \int_{\partial\Omega} \sigma \frac{\partial}{\partial n} F_D^\sigma \gamma_D F_R^\sigma(f) \cdot \gamma_D F_D^\sigma(g) ds + \alpha \int_{\partial\Omega} \gamma_D F_R^\sigma(f) \cdot \gamma_D F_D^\sigma(g) ds \tag{3.26}$$

$$= \int_{\partial\Omega} (\sigma \frac{\partial}{\partial n} F_D^\sigma \gamma_D F_R^\sigma(f) + \alpha \gamma_D F_R^\sigma(f)) \cdot \gamma_D F_D^\sigma(g) ds \tag{3.27}$$

$$= \int_{\partial\Omega} (\left(\sigma \frac{\partial}{\partial n} + \alpha\gamma_D\right) F_R^\sigma(f)) \cdot \gamma_D F_D^\sigma(g) ds \tag{3.28}$$

$$= \int_{\partial\Omega} f \gamma_D F_D^\sigma g ds \tag{3.29}$$

$$= \int_{\partial\Omega} f g ds. \tag{3.30}$$

First we express the first integral in terms of a duality pairing in (3.26). Then we combine both integrals in (3.27) and apply the identities (3.8) and (3.6) to get to (3.28) and (3.29). Since g is defined on $H_\sigma^{1/2}$, applying the Dirichlet extension operator followed by the Dirichlet trace leads back to g. (identity (3.5))

At this point we cannot continue in an intuitive way so we go on by looking at the other side of the defining equality:

$$< f, A^* g >_{H_\sigma^{-1/2}} = \int_\Omega \sigma \nabla F_R^\sigma(f) \cdot \nabla F_R^\sigma(A^* g) dx + \alpha \int_{\partial\Omega} \gamma_D F_R^\sigma(f) \cdot \gamma_D F_R^\sigma(A^* g) ds \tag{3.31}$$

$$= \int_{\partial\Omega} \sigma \frac{\partial}{\partial n} F_R^\sigma(f) \cdot \gamma_D F_R^\sigma(A^* g) ds + \alpha \int_{\partial\Omega} \gamma_D F_R^\sigma(f) \cdot \gamma_D F_R^\sigma(A^* g) ds \tag{3.32}$$

$$= \int_{\partial\Omega} (\left(\sigma \frac{\partial}{\partial n} + \alpha\gamma_D\right) F_R^\sigma(f)) \cdot \gamma_D F_R^\sigma(A^* g) ds \tag{3.33}$$

$$= \int_{\partial\Omega} f \cdot \gamma_D F_R^\sigma(A^* g) ds. \tag{3.34}$$

The steps are similar to those of the other inner product. After writing down the definition of the inner product, we use a duality pairing in (3.32), combine the integrals in (3.33) and use identity (3.6) in (3.34).

Now the inner products are in a form that allows us to compare both sides. Since $< Af, g >=< f, A^*g >$ has to hold for all $f \in H_\sigma^{-1/2}, g \in H_\sigma^{1/2}$ and we were able to isolate f, the other parts of the duality pairings have to equal each other as well.

So we have:

$$g = \gamma_D F_R^\sigma A^* g \tag{3.35}$$

$$\gamma_D F_R^\sigma \left(\sigma \frac{\partial}{\partial n} + \alpha \gamma_D\right) F_D^\sigma g = \gamma_D F_R^\sigma A^* g \tag{3.36}$$

$$\left(\sigma \frac{\partial}{\partial n} + \alpha \gamma_D\right) F_D^\sigma g = A^* g. \tag{3.37}$$

First we apply identity (3.10) in (3.36) in order to allow us to cancel the Dirichlet trace and Robin extension in (3.37). The cancellation is justified because the Robin-to-Dirichlet map is injective.

We have now found the desired expression for A^*:

$$A^* : g \mapsto \left(\sigma \frac{\partial}{\partial n} + \alpha \gamma_D\right) F_D^\sigma g \tag{3.38}$$

Note that A is no longer self-adjoint for this choice of spaces.

3.3.3 $i_+ : H_{\sigma_*}^{1/2} \to H_{\sigma_0}^{1/2}$

The following operators are all inclusions, so $i_+ f = f$. However the adjoint is non-trivial. On one side the steps are as follows:

$$< i_+ f, g >_{H_{\sigma_0}^{1/2}} = \int_\Omega \sigma_0 \nabla F_D^{\sigma_0} f \cdot \nabla F_D^{\sigma_0} g dx + \alpha \int_{\partial\Omega} \gamma_D F_D^{\sigma_0} f \cdot \gamma_D F_D^{\sigma_0} g ds \tag{3.39}$$

$$= \int_\Omega \gamma_D F_D^{\sigma_0} f \cdot \sigma_0 \frac{\partial}{\partial n} F_D^{\sigma_0} g dx + \alpha \int_{\partial\Omega} \gamma_D F_D^{\sigma_0} f \cdot \gamma_D F_D^{\sigma_0} g ds \tag{3.40}$$

$$= \int_{\partial\Omega} \gamma_D F_D^{\sigma_0} f \left(\sigma_0 \frac{\partial}{\partial n} + \alpha \gamma_D\right) F_D^{\sigma_0} g ds \tag{3.41}$$

$$= \int_{\partial\Omega} f \left(\sigma_0 \frac{\partial}{\partial n} + \alpha \gamma_D\right) F_D^{\sigma_0} g ds. \tag{3.42}$$

(3.40) uses the duality pairing, (3.41) combines both integrals and (3.42) makes use of identity (3.5).

The same steps can be performed on the other side of the inclusion operator since the spaces are essentially the same except for the differing σ. Therefore we have:

$$< f, i_+^* g >_{H_{\sigma_*}^{1/2}} = \int_{\partial\Omega} f \left(\sigma_* \frac{\partial}{\partial n} + \alpha\gamma_D \right) F_D^{\sigma_*} i_+^* g ds. \tag{3.43}$$

Since the defining equation for the adjoint operator has to hold for all f and g, we can compare both sides again:

$$\left(\sigma_0 \frac{\partial}{\partial n} + \alpha\gamma_D \right) F_D^{\sigma_0} g = \left(\sigma_* \frac{\partial}{\partial n} + \alpha\gamma_D \right) F_D^{\sigma_*} i_+ g \tag{3.44}$$

$$\left(\sigma_* \frac{\partial}{\partial n} + \alpha\gamma_D \right) F_D^{\sigma_*} \gamma_D F_R^{\sigma_*} \left(\sigma_0 \frac{\partial}{\partial n} + \alpha\gamma_D \right) F_D^{\sigma_0} g = \left(\sigma_* \frac{\partial}{\partial n} + \alpha\gamma_D \right) F_D^{\sigma_*} i_+ g \tag{3.45}$$

$$\gamma_D F_R^{\sigma_*} \left(\sigma_0 \frac{\partial}{\partial n} + \alpha\gamma_D \right) F_D^{\sigma_0} g = i_+ g. \tag{3.46}$$

The step (3.45) uses identity (3.9) with $\sigma = \sigma_*$ and the cancellation in (3.46) is allowed because the operators are injective.

Now we have the expression for i_+ that we were looking for:

$$i_+^* : g \mapsto \gamma_D F_R^{\sigma_*} \left(\sigma_0 \frac{\partial}{\partial n} + \alpha\gamma_D \right) F_D^{\sigma_0} g. \tag{3.47}$$

3.3.4 $i_- : H_{\sigma_0}^{-1/2} \to H_{\sigma_*}^{-1/2}$

The operator i_- is an embedding operator, so $i_- f = f$. On one side:

$$< i_- f, g >_{H_{\sigma_*}^{-1/2}} = \int_\Omega \sigma_* \nabla F_R^{\sigma_*} f \cdot \nabla F_R^{\sigma_*} g dx + \alpha \int_{\partial\Omega} \gamma_D F_R^{\sigma_*} f \gamma_D F_R^{\sigma_*} g ds \tag{3.48}$$

$$= \int_{\partial\Omega} \sigma_* \frac{\partial}{\partial n} F_R^{\sigma_*} f \gamma_D F_R^{\sigma_*} g ds + \alpha \int_{\partial\Omega} \gamma_D F_R^{\sigma_*} f \gamma_D F_R^{\sigma_*} g ds \tag{3.49}$$

$$= \int_{\partial\Omega} \left(\sigma_* \frac{\partial}{\partial n} + \alpha\gamma_D \right) F_R^{\sigma_*} f \gamma_D F_R^{\sigma_*} g ds \tag{3.50}$$

$$= \int_{\partial\Omega} f \gamma_D F_R^{\sigma_*} g ds. \tag{3.51}$$

Just like before, (3.49) uses the duality pairing and (3.50) combines the integrals. (3.51) uses identity (3.6).

The other inner product is the same except for a different σ again, so the exact same steps can be used to obtain:

$$< f, i_-^* g >_{H_{\sigma_0}^{-1/2}} = \int_{\partial\Omega} f \gamma_D F_R^{\sigma_0} i_-^* g ds. \tag{3.52}$$

Since one argument of the duality pairing is the same for both sides, the other ones have to match too, thus:

$$\gamma_D F_R^{\sigma^*} g = \gamma_D F_R^{\sigma_0} i_-^* g \tag{3.53}$$

$$\gamma_D F_R^{\sigma_0} \left(\sigma_0 \frac{\partial}{\partial n} + \alpha \gamma_D \right) F_D^{\sigma_0} \gamma_D F_R^{\sigma^*} g = \gamma_D F_R^{\sigma_0} i_-^* g \tag{3.54}$$

$$\left(\sigma_0 \frac{\partial}{\partial n} + \alpha \gamma_D \right) F_D^{\sigma_0} \gamma_D F_R^{\sigma^*} g = i_-^* g. \tag{3.55}$$

Equation (3.54) is obtained using identity (3.10) and we end up with (3.55) using cancellation.

So i_-^* is given by:

$$i_-^* : g \mapsto \left(\sigma_0 \frac{\partial}{\partial n} + \alpha \gamma_D \right) F_D^{\sigma_0} \gamma_D F_R^{\sigma^*} g. \tag{3.56}$$

3.3.5 $I_-^\sigma : \quad L_2 \hookrightarrow H_\sigma^{-1/2}$

The steps to find $(I_-^\sigma)^*$ are similar to the steps used to find the other adjoint operators.

$$< I_-^\sigma f, g >_{H_\sigma^{-1/2}} = \int_\Omega \sigma \nabla F_R^\sigma f \cdot \nabla F_R^\sigma g dx + \alpha \int_{\partial\Omega} \gamma_D F_R^\sigma f \cdot \gamma_D F_R^\sigma g ds \tag{3.57}$$

$$= \int_{\partial\Omega} \left(\sigma \frac{\partial}{\partial n} + \alpha \gamma_D \right) F_R^\sigma f \cdot \gamma_D F_R^\sigma g ds \tag{3.58}$$

$$= \int_{\partial\Omega} f \cdot \gamma_D F_R^\sigma g ds. \tag{3.59}$$

After applying the definition of the inner product, (3.58) uses the duality pairing and combines the integral. Step (3.59) is identity (3.6). Note that this resulting duality pairing can also be understood as an L_2 inner product because $\gamma_D F_R^\sigma g$ is in $H_\sigma^{1/2} \subset L_2$.

The other side is just the L_2 inner product, so:

$$< f, (I_-^\sigma)^* g >_{L_2} = \int_{\partial\Omega} f \cdot (I_-^\sigma)^* g ds. \tag{3.60}$$

The comparison of both integrals immediately leads to:

$$(I_-^\sigma)^* : g \mapsto \gamma_D F_R^\sigma g. \tag{3.61}$$

3.3.6 $I_+^\sigma : \quad H_\sigma^{1/2} \hookrightarrow L_2$

This calculation again follows the same idea to find the adjoint.

$$< I_+^\sigma f, g >_{L_2} = \int_{\partial\Omega} f \cdot g ds. \tag{3.62}$$

Note that this can also be interpreted as a duality pairing because $f \in H_\sigma^{1/2}$ and $g \in L_2 \subset H_\sigma^{-1/2}$.

The domain of I_+^σ is $H_\sigma^{1/2}$, so we need the other inner product:

$$< f, (I_+^\sigma)^* g >_{H_\sigma^{1/2}} = \int_\Omega \sigma \nabla F_D^\sigma f \cdot \nabla F_D^\sigma (I_+^\sigma)^* g dx + \alpha \int_{\partial\Omega} \gamma_D F_D^\sigma f \cdot \gamma_D F_D^\sigma (I_+^\sigma)^* g ds \tag{3.63}$$

$$= \int_{\partial\Omega} \gamma_D F_D^\sigma f \cdot \left(\sigma \frac{\partial}{\partial n} + \alpha \gamma_D \right) F_D^\sigma (I_+^\sigma)^* g ds \tag{3.64}$$

$$= \int_{\partial\Omega} f \cdot \left(\sigma \frac{\partial}{\partial n} + \alpha \gamma_D \right) F_D^\sigma (I_+^\sigma)^* g ds. \tag{3.65}$$

Again, (3.64) uses the duality pairing and joins the integrals; (3.65) uses identity (3.5). Now

we have to compare both sides again, just like for the other adjoint calculations:

$$g = \left(\sigma\frac{\partial}{\partial n} + \alpha\gamma_D\right) F_D^\sigma (I_+^\sigma)^* g \tag{3.66}$$

$$\left(\sigma\frac{\partial}{\partial n} + \alpha\gamma_D\right) F_D^\sigma \gamma_D F_R^\sigma g = \left(\sigma\frac{\partial}{\partial n} + \alpha\gamma_D\right) F_D^\sigma (I_+^\sigma)^* g \tag{3.67}$$

$$\gamma_D F_R^\sigma = (I_+^\sigma)^*. \tag{3.68}$$

First we apply identity (3.9) and then we cancel the Robin trace and the Dirichlet extension on both sides, giving us the result

$$(I_+^\sigma)^* : g \mapsto \gamma_D F_R^\sigma g. \tag{3.69}$$

This finalizes the calculations of the basic adjoint operators. □

3.4 Compound adjoints

Now that we have all relevant adjoints that are used to define the distinguishability criteria, we can put them together using basic properties of adjoint operators.

Lemma 3. *For Hilbert spaces $\mathcal{H}_1, \mathcal{H}_2, \mathcal{H}_3$ and operators $a, b : \mathcal{H}_1 \to \mathcal{H}_2$ and $c : \mathcal{H}_2 \to \mathcal{H}_3$ with adjoints a^*, b^*, c^*, the following equalities hold:*

$$(a+b)^* = a^* + b^* \tag{3.70}$$

$$(cb)^* = b^* c^* \tag{3.71}$$

Proof. For the first identity

$$< (a+b)f, g > =< af + bf, g >=< af, g > + < bf, g >= \tag{3.72}$$

$$=< f, a^* g > + < f, b^* g >=< f, a^* g + b^* g >=< f, (a^* + b^*) g > \tag{3.73}$$

$$=< f, (a+b)^* g > . \tag{3.74}$$

The last equality holds because of the defining property of the adjoint operator.

For the second identity:

$$< (bc)f, g > =< cf, b^* g >=< f, c^* b^* g > \tag{3.75}$$

$$=< f, (bc)^* g > . \tag{3.76}$$

And again, the last step is using the definition of the adjoint. □

Theorem 2. *For the distinguishability criteria:*

$$A_1 : L_2 \to L_2 : \qquad j \mapsto \gamma_D F_R^{\sigma_0}(j) - \gamma_D F_R^{\sigma_*}(j) \tag{3.77}$$

$$A_2 : H_{\sigma_0}^{-1/2} \to H_{\sigma_0}^{1/2} : \qquad j \mapsto \gamma_D F_R^{\sigma_0}(j) - i_+ \gamma_D F_R^{\sigma_*} i_-(j) \tag{3.78}$$

$$A_3 : L_2 \to H_{\sigma_0}^{1/2} : \qquad j \mapsto \gamma_D F_R^{\sigma_0} I_-^{\sigma_0}(j) - i_+ \gamma_D F_R^{\sigma_*} i_- I_-^{\sigma_0}(j) \tag{3.79}$$

$$A_4 : H_{\sigma_0}^{-1/2} \to L_2 : \qquad j \mapsto I_+^{\sigma_0} \gamma_D F_R^{\sigma_0}(j) - I_+^{\sigma_0} i_+ \gamma_D F_R^{\sigma_*} i_-(j). \tag{3.80}$$

The adjoints are given by:

$$A_1^* = A_1 \tag{3.81}$$

$$A_2^* = \left(\sigma_0 \frac{\partial}{\partial n} + \alpha \gamma_D \right) F_D^{\sigma_0} (id_D - \tilde{E}) \tag{3.82}$$

$$A_3^* = id_D - \tilde{E} \tag{3.83}$$

$$A_4^* = id_R - E \tag{3.84}$$

where:

$$E = \left(\sigma_0 \frac{\partial}{\partial n} + \alpha \gamma_D \right) F_D^{\sigma_0} \gamma_D F_R^{\sigma_*} \tag{3.85}$$

$$\tilde{E} = \gamma_D F_R^{\sigma_*} \left(\sigma_0 \frac{\partial}{\partial n} + \alpha \gamma_D \right) F_D^{\sigma_0}. \tag{3.86}$$

Note that: $\gamma_D F_R^{\sigma_*} E = \tilde{E} \gamma_D F_R^{\sigma_*}$

And the essential part of the Power Method iteration $A_k^* A_k, k \in \{1,2,3,4\}$ is given by:

$$A_1^* A_1 = A_1^2 \tag{3.87}$$

$$A_2^* A_2 = (id_R - E)^2 \tag{3.88}$$

$$A_3^* A_3 = (id_D - \tilde{E}) A_3 \tag{3.89}$$

$$A_4^* A_4 = (id_R - E) A_4. \tag{3.90}$$

Proof. The main tool to prove this theorem is using the identities that are obtained at the beginning of this chapter:

3.4.1 $A_1 : L_2 \to L_2 : \quad j \mapsto \gamma_D F_R^{\sigma_0}(j) - \gamma_D F_R^{\sigma_*}(j)$

Since $(\gamma_D F_R^{\sigma})$ is self-adjoint, A_1 is also self-adjoint, so we immediately get:

$$A_1^* = A_1 = \gamma_D F_R^{\sigma_0} - \gamma_D F_R^{\sigma_*}. \tag{3.91}$$

3.4.2 $A_2 : H_{\sigma_0}^{-1/2} \to H_{\sigma_0}^{1/2} : \quad j \mapsto \gamma_D F_R^{\sigma_0}(j) - i_+ \gamma_D F_R^{\sigma_*} i_-(j)$

The calculations for A_2 are as follows:

$$\begin{aligned}
A_2^* =& (\gamma_D F_R^{\sigma_0} - i_+ \gamma_D F_R^{\sigma_*} i_-)^* && (3.92)\\
=& (F_R^{\sigma_0})^* (\gamma_D)^* - (i_-)^* (F_R^{\sigma_*})^* (\gamma_D)^* (i_+)^* && (3.93)\\
=& \left(\sigma_0 \frac{\partial}{\partial n} + \alpha \gamma_D\right) F_D^{\sigma_0} \\
& - \left(\sigma_0 \frac{\partial}{\partial n} + \alpha \gamma_D\right) F_D^{\sigma_0} \gamma_D F_R^{\sigma_0} \left(\sigma_* \frac{\partial}{\partial n} + \alpha \gamma_D\right) F_D^{\sigma_*} \gamma_D F_R^{\sigma_*} \left(\sigma_0 \frac{\partial}{\partial n} + \alpha \gamma_D\right) F_R^{\sigma_0} && (3.94)\\
=& \left(\sigma_0 \frac{\partial}{\partial n} + \alpha \gamma_D\right) F_D^{\sigma_0} (id_D - \gamma_D F_R^{\sigma_*} \left(\sigma_* \frac{\partial}{\partial n} + \alpha \gamma_D\right) F_D^{\sigma_*} \gamma_D F_R^{\sigma_*} \left(\sigma_0 \frac{\partial}{\partial n} + \alpha \gamma_D\right) F_D^{\sigma_0}) \\
& && (3.95)\\
=& \left(\sigma_0 \frac{\partial}{\partial n} + \alpha \gamma_D\right) F_D^{\sigma_0} (id_D - \gamma_D F_R^{\sigma_*} \left(\sigma_0 \frac{\partial}{\partial n} + \alpha \gamma_D\right) F_D^{\sigma_0}) && (3.96)\\
=& \left(\sigma_0 \frac{\partial}{\partial n} + \alpha \gamma_D\right) F_D^{\sigma_0} (id_D - \tilde{E}). && (3.97)
\end{aligned}$$

In (3.94), the adjoints are evaluated, then the bracket is distributed in (3.95) and finally, identity (3.9) is used in (3.96).

$A_2^* A_2$ can easily be calculated:

$$A_2^* A_2 = \left(\sigma_0 \frac{\partial}{\partial n} + \alpha\gamma_D\right) F_D^{\sigma_0}(id_D - \tilde{E})(\gamma_D F_R^{\sigma_0} - \gamma_D F_R^{\sigma_*}) \tag{3.98}$$

$$= \left(\sigma_0 \frac{\partial}{\partial n} + \alpha\gamma_D\right) F_D^{\sigma_0}(\gamma_D F_R^{\sigma_0} - \gamma_D F_R^{\sigma_*} - \tilde{E}\gamma_D F_R^{\sigma_0} + \tilde{E}\gamma_D F_R^{\sigma_*}) \tag{3.99}$$

$$= id_R - E - E + E^2 \tag{3.100}$$

$$= (id_R - E)^2. \tag{3.101}$$

The step (3.99) is expanding the bracket and (3.100) uses the identities (3.9) and (3.10).

3.4.3 $A_3 : L_2 \to H_{\sigma_0}^{1/2} : \quad j \mapsto \gamma_D F_R^{\sigma_0} I_-^{\sigma_0}(j) - i_+ \gamma_D F_R^{\sigma_*} i_- I_-^{\sigma_0}(j)$

These are the calculations for A_3^*:

$$\begin{aligned} A_3^* =& \gamma_D F_R^{\sigma_0} \left(\sigma_0 \frac{\partial}{\partial n} + \alpha\gamma_D\right) F_D^{\sigma_0} \\ & - \gamma_D F_R^{\sigma_0} \left(\sigma_0 \frac{\partial}{\partial n} + \alpha\gamma_D\right) F_D^{\sigma_0} \gamma_D F_R^{\sigma_*} \left(\sigma_* \frac{\partial}{\partial n} + \alpha\gamma_D\right) F_D^{\sigma_*} \gamma_D F_R^{\sigma_*} \left(\sigma_0 \frac{\partial}{\partial n} + \alpha\gamma_D\right) F_D^{\sigma_0} \end{aligned} \tag{3.102}$$

$$= id_D - \tilde{E}. \tag{3.103}$$

After assembling the adjoint in (3.102) the identity (3.10) is used in (3.103). There are no reasonable simplifications to optimize the numerical properties of the Power Method iteration in this case, so the simplest expression is:

$$A_3^* A_3 = (id_D - \tilde{E}) A_3. \tag{3.104}$$

3.4.4 $A_4 : H_{\sigma_0}^{-1/2} \to L_2 : \quad j \mapsto I_+^{\sigma_0}\gamma_D F_R^{\sigma_0}(j) - I_+^{\sigma_0} i_+ \gamma_D F_R^{\sigma_*} i_-(j)$

The steps needed to calculate A_4^* are about the same:

$$\begin{aligned} A_4^* = &\left(\sigma_0 \frac{\partial}{\partial n} + \alpha\gamma_D\right) F_D^{\sigma_0}\gamma_D F_R^{\sigma_0} \\ &- \left(\sigma_0 \frac{\partial}{\partial n} + \alpha\gamma_D\right) F_D^{\sigma_0}\gamma_D F_R^{\sigma_*} \left(\sigma_* \frac{\partial}{\partial n} + \alpha\gamma_D\right) F_D^{\sigma_*}\gamma_D F_R^{\sigma_*} \left(\sigma_0 \frac{\partial}{\partial n} + \alpha\gamma_D\right) F_D^{\sigma_0}\gamma_D F_R^{\sigma_0} \end{aligned} \tag{3.105}$$

$$= id_R - E. \tag{3.106}$$

Unfortunately, this distinguishability also has no further reasonable simplification.

$$A_4^* A_4 = (id_R - E)A_4. \tag{3.107}$$

This finalizes the calculation of all four distinguishability criteria. □

If we replace the Robin-Problem with the Neumann-Problem, all calculations will stay the same except for the nonexistent α-term and the additionally necessary validation of the integrability condition (2.9). For more information about the NtD problem, see [4].

Chapter 4

Numerical simulations

This chapter presents the numerical results.

4.1 Algorithm

All computations are performed in MATLAB. The Partial Differential Equations toolbox provides the necessary tools to approximate the extension operators and calculate the norms, thus the Power Method can be almost directly implemented.

The typical test problems used to examine the difference between the distinguishability criteria in this thesis consist of the guess σ_0 being a homogenous background with a value of $\sigma_0 = 5.5$ and the distribution σ_* consisting of one small circular inclusion with a peak of 9 times the background value added to σ_0. The domain Ω is a disk with radius one, consequently the inclusions will usually have a radius around 0.2. The parameter α of the Robin problem's boundary condition should be chosen to have the same order of magnitude as the Neumann-part, which is hard to estimate. In cases of no further indication, α is chosen to be one.

Due to the exponentially fast converging nature of the Power Method, 100 iterations are usually sufficient for the problem to converge. However for this thesis a minimum of 250 iterations are used until termination of the Power Method.

The problems are discretized using the piecewise linear finite element method. The results seem to be stable with respect to the mesh parameters, however in the calculations of this thesis the mesh is usually triangularized into 4128 finite elements to keep the code evaluation time at a reasonable level.

For each space-setting, four extensions are needed to evaluate A^*A, as discussed in the previous chapter. The NtD problem is also implemented; the only parts of the code that change for the NtD optimization are the traces and extension operators, everything else stays the same, agreeing with [4].

4.2 Comparison criteria

It is by no means easy to decide if a current that is optimal with respect to a space combination is better or worse than one that is optimal with respect to a different choice of spaces, therefore it is necessary to find criteria to compare the results.

4.2.1 Eigenvalues as a comparison criterion

A very dominant optimal current results in the possibility of fast extraction of information about the conductivity inside the domain and more importantly, an eigenvector with a large eigenvalue is also more likely to drown the noise of the physical setup, therefore a big eigenvalue is desired.

4.2.2 Localization Measure of eigenfunctions

A useful tool that is used for the reconstruction of σ_* is the sharpness and position of the eigenfunction's localization, implying that for the case of one inclusion close to the boundary, an optimal current that quickly decays to zero when moving away from the angle of the inclusion is preferable when running a routine to approximate σ_*. This can be quantitized in the following manner: [3]

For each normalized k-th optimal current j_k, the value $j_k(\theta), -\pi \leq \theta \leq \pi$ is com-

puted during the optimization routine. We then can interpret the current distribution as a probability density function by defining

$$p_k(\theta) = \frac{|j_k(\theta)|}{\int_{-\pi}^{\pi} |j_k(\theta)| d\theta}. \tag{4.1}$$

It is thus desirable that the expected value $\bar{\theta}_k$ of this probability distribution is close to the actual angle $\hat{\theta}$ of the inclusion. Therefore a quantity that allows us to distinguish between the performances of the optimal currents is given by:

$$Err(\bar{\theta}_k) = |\bar{\theta}_k - \hat{\theta}| = |\int_{-\pi}^{\pi} \theta p_k(\theta) d\theta - \hat{\theta}|. \tag{4.2}$$

The variance of p is a measure of the current's sharpness, therefore it is appropriate to use

$$var_k(\theta) = \int_{-\pi}^{\pi} (\theta - \bar{\theta}_k)^2 p_k(\theta) d\theta \tag{4.3}$$

to determine whether or not an optimal current has good properties.

4.3 Examples

This part is going to present a few examples for optimal currents.

The following table summarizes the parameters for each set of example optimizations:

Table 4.1: Parameters of example problems

	Example							
Parameter	1	2	3	4	5	6	7	8
Algorithm settings								
Iterations	100	100	100	100	100	100	100	500
α	1	1	1	1	1	10	1	1
σ_0	5.5	5.5	5.5	5.5	5.5	5.5	2	5.5
triangles of mesh	4128	4128	4128	4128	4128	4128	4128	16512
Properties of σ_*'s inclusion								
position	$-\frac{\pi}{4}$	$\frac{3\pi}{7}$	$-\frac{\pi}{4}$	$-\frac{\pi}{4}$	$-\frac{\pi}{4}$	$-\frac{\pi}{4}$	$-\frac{\pi}{4}$	$-\frac{\pi}{4}$
distance from center	0.6	0.6	0.1	0.6	0.6	0.6	0.6	0.6
radius	0.2	0.2	0.2	0.3	0.2	0.2	0.2	0.2
peak ($\cdot\sigma_0$)	10	10	10	10	20	10	10	10

The first example will be a reference point and all other examples will change one particular parameter.

Figure 4.1: Example 1 - Reference example: All optimal currents with the three biggest eigenvalues converge for all four space combinations. Cases c and d does not give meaningful results; all other spaces are able to localize the inclusion at $-\frac{\pi}{4}$. g andh have the sharpest localization, while a and b have the smoothest. The patterns for a fixed space setting is similar, but the Robin settings generally have sharper localizations.

(a) $L_2 \to L_2$ Robin

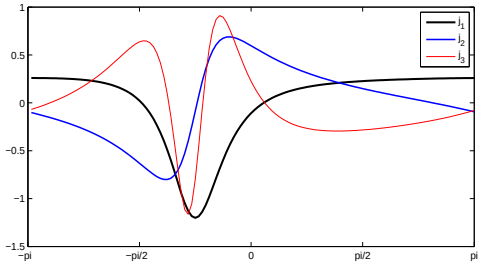

(b) $L_2 \to L_2$ Neumann

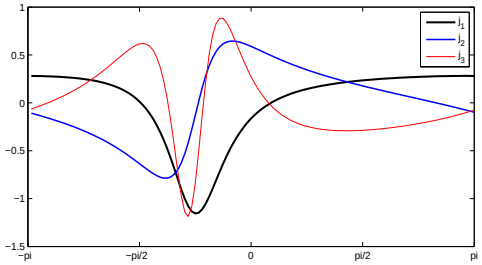

(c) $H_{\sigma_0}^{-1/2} \to H_{\sigma_0}^{1/2}$ Robin

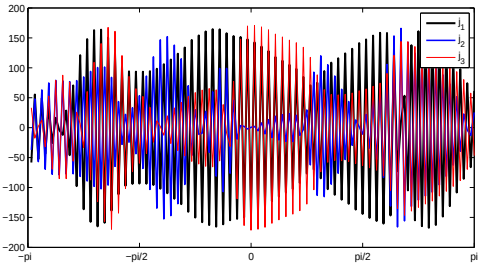

(d) $H_{\sigma_0}^{-1/2} \to H_{\sigma_0}^{1/2}$ Neumann

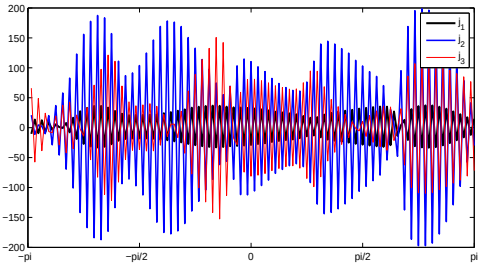

(e) $L_2 \to H_{\sigma_0}^{1/2}$ Robin

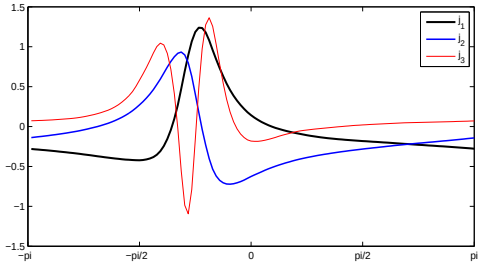

(f) $L_2 \to H_{\sigma_0}^{1/2}$ Neumann

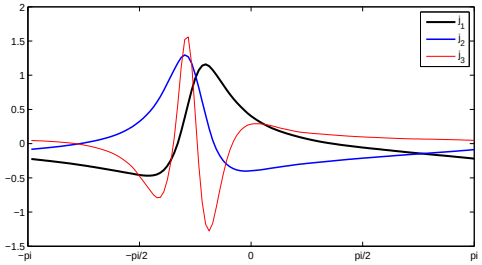

(g) $H_{\sigma_0}^{-1/2} \to L_2$ Robin

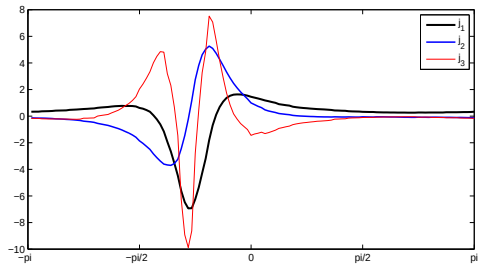

(h) $H_{\sigma_0}^{-1/2} \to L_2$ Neumann

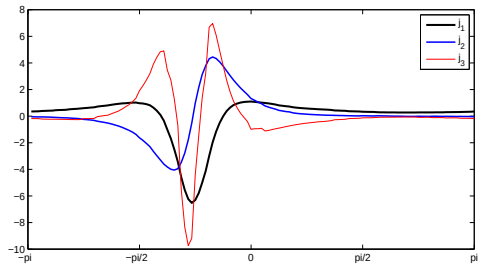

	λ_1	λ_2	λ_3
Robin-to-Dirichlet			
$L_2 \to L_2$	2.19e-004	2.11e-004	1.11e-006
$H_{\sigma_0}^{-1/2} \to H_{\sigma_0}^{1/2}$	9.95e-001	9.83e-001	9.93e-001
$L_2 \to H_{\sigma_0}^{1/2}$	2.38e-003	2.39e-003	7.60e-004
$H_{\sigma_0}^{-1/2} \to L_2$	2.47e-003	2.45e-003	1.47e-004
Neumann-to-Dirichlet			
$L_2 \to L_2$	3.54e-004	3.42e-004	1.51e-006
$H_{\sigma_0}^{-1/2} \to H_{\sigma_0}^{1/2}$	1.01e+000	9.94e-001	9.86e-001
$L_2 \to H_{\sigma_0}^{1/2}$	3.26e-003	3.21e-003	4.51e-004
$H_{\sigma_0}^{-1/2} \to L_2$	3.36e-003	3.31e-003	2.26e-004

Table 4.2: Example 1 - Reference example: Eigenvalues: $H_{\sigma_0}^{-1/2} \to L_2$ has the biggest eigenvalues, $L_2 \to H_{\sigma_0}^{1/2}$ the second biggest, $L_2 \to L_2$ the smallest. $H_{\sigma_0}^{-1/2} \to H_{\sigma_0}^{1/2}$ should be ignored because the shape of the result is impractical. The eigenvalues for the Neumann settings are slightly better but follow the same trend.

	$Err(\bar{\theta}_1)$	$Err(\bar{\theta}_2)$	$Err(\bar{\theta}_3)$	$var_1(\theta)$	$var_2(\theta)$	$var_3(\theta)$
Robin-to-Dirichlet						
$L_2 \to L_2$	0.078	0.106	0.195	2.533	1.460	2.095
$H_{\sigma_0}^{-1/2} \to H_{\sigma_0}^{1/2}$	0.095	0.050	0.162	3.219	3.810	3.457
$L_2 \to H_{\sigma_0}^{1/2}$	0.300	0.442	0.252	2.266	1.950	0.872
$H_{\sigma_0}^{-1/2} \to L_2$	0.063	0.112	0.011	1.283	0.592	0.623
Neumann-to-Dirichlet						
$L_2 \to L_2$	0.101	0.135	0.187	2.613	1.572	2.118
$H_{\sigma_0}^{-1/2} \to H_{\sigma_0}^{1/2}$	0.094	0.106	0.231	3.225	3.314	3.136
$L_2 \to H_{\sigma_0}^{1/2}$	0.310	0.311	0.130	1.617	1.724	1.164
$H_{\sigma_0}^{-1/2} \to L_2$	0.001	0.017	0.019	1.374	0.456	0.663

Table 4.3: Example 1 - Reference example: Localizations: The localization parameters share the ranking with the eigenvalues for the spaces, but this time the Robin settings generally perform better. $Err(\theta_k)$ does not allow good conclusions and $var(\theta_k)$ is very noisy. However, the trend is apparent.

4.3.1 Discussion of example 1

The first thing that is apparent is the fact that both $H_{\sigma_0}^{-1/2} \to H_{\sigma_0}^{1/2}$ space combinations do not converge. This is due to the lack of smoothing parts of the Power Method's iteration and this result is consistent with the results from [4]. For this space, the current value changes its sign at each edge and the rerun of the algorithm with a different initial guess converges to a different result. The optimal currents for these choices of spaces seem to have no connection to the conductivity σ_*. For completeness this choice of spaces is displayed in the further examples even though it is not a reasonable choice for any application.

The other space combinations show the desired localization near the actual angle of the inclusion. $L_2 \to L_2$ has the smoothest localization and $H_{\sigma_0}^{-1/2} \to L_2$ the sharpest. The values of $Err(\theta)$ and $var(\theta)$ agree with this observation.

The eigenvalues of the $L_2 \to L_2$ settings are smallest, $H_{\sigma_0}^{-1/2} \to L_2$ and $L_2 \to H_{\sigma_0}^{1/2}$ have almost the same eigenvalues, where the latter is marginally better.

The Neumann results are very similar to the Robin results. However there are a few apparent differences: The eigenvalues of the Neumann setup are slightly better and the localization is slightly worse, but both boundary conditions share the same characteristics for equal space combinations, e.g. the sharpness.

Figure 4.2: Example 2 - Different angle: The algorithm clearly shows the same behavior for a different angle. The current patterns have the same shape but are now localized near $\frac{3\pi}{7}$.

(a) $L_2 \to L_2$ Robin

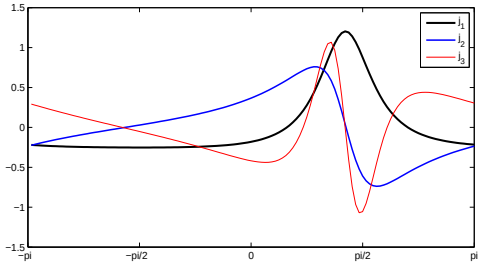

(b) $L_2 \to L_2$ Neumann

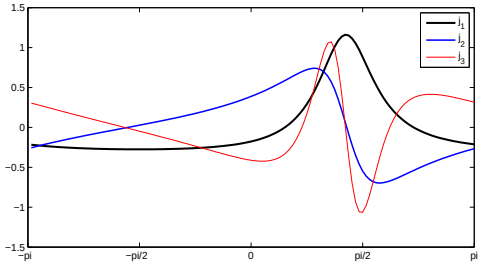

(c) $H_{\sigma_0}^{-1/2} \to H_{\sigma_0}^{1/2}$ Robin

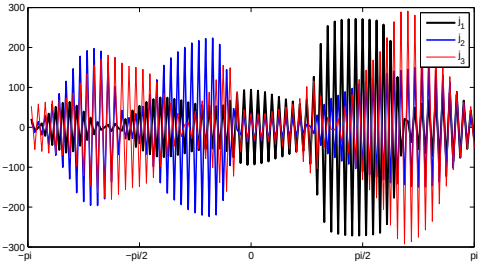

(d) $H_{\sigma_0}^{-1/2} \to H_{\sigma_0}^{1/2}$ Neumann

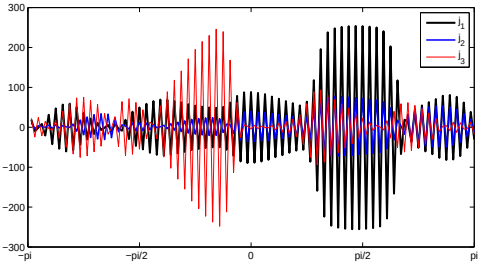

(e) $L_2 \to H_{\sigma_0}^{1/2}$ Robin

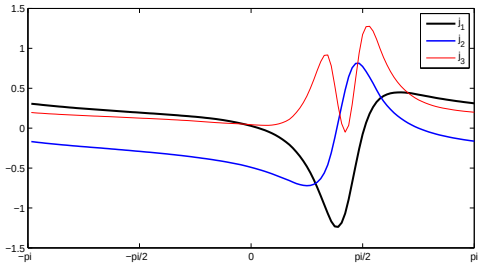

(f) $L_2 \to H_{\sigma_0}^{1/2}$ Neumann

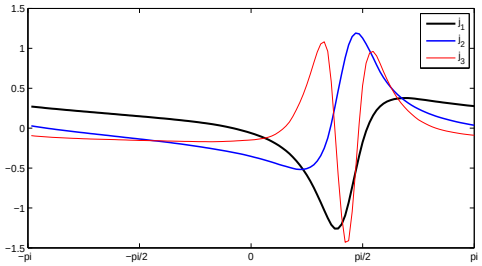

(g) $H_{\sigma_0}^{-1/2} \to L_2$ Robin

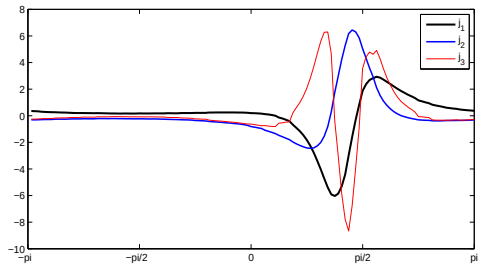

(h) $H_{\sigma_0}^{-1/2} \to L_2$ Neumann

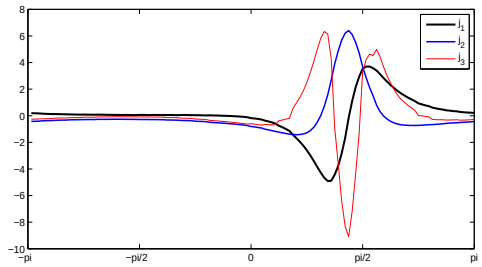

	λ_1	λ_2	λ_3
Robin-to-Dirichlet			
$L_2 \to L_2$	2.24e-004	2.16e-004	1.12e-006
$H_{\sigma_0}^{-1/2} \to H_{\sigma_0}^{1/2}$	9.99e-001	9.95e-001	9.88e-001
$L_2 \to H_{\sigma_0}^{1/2}$	2.47e-003	2.36e-003	1.43e-003
$H_{\sigma_0}^{-1/2} \to L_2$	2.56e-003	2.48e-003	1.80e-004
Neumann-to-Dirichlet			
$L_2 \to L_2$	3.62e-004	3.49e-004	1.52e-006
$H_{\sigma_0}^{-1/2} \to H_{\sigma_0}^{1/2}$	9.99e-001	1.00e+000	9.88e-001
$L_2 \to H_{\sigma_0}^{1/2}$	3.36e-003	3.20e-003	5.65e-004
$H_{\sigma_0}^{-1/2} \to L_2$	3.43e-003	3.39e-003	2.85e-004

Table 4.4: Example 2 - Different angle: Eigenvalues: The eigenvalues follow the same trend as in the reference example and are almost the same value.

	$Err(\bar{\theta}_1)$	$Err(\bar{\theta}_2)$	$Err(\bar{\theta}_3)$	$var_1(\theta)$	$var_2(\theta)$	$var_3(\theta)$
Robin-to-Dirichlet						
$L_2 \to L_2$	0.038	0.028	0.007	2.562	1.442	1.750
$H_{\sigma_0}^{-1/2} \to H_{\sigma_0}^{1/2}$	0.145	0.061	0.285	1.704	3.713	3.105
$L_2 \to H_{\sigma_0}^{1/2}$	0.300	0.447	0.342	2.139	2.343	1.583
$H_{\sigma_0}^{-1/2} \to L_2$	0.146	0.150	0.017	0.901	1.085	0.639
Neumann-to-Dirichlet						
$L_2 \to L_2$	0.054	0.049	0.023	2.657	1.548	1.789
$H_{\sigma_0}^{-1/2} \to H_{\sigma_0}^{1/2}$	0.144	0.189	0.820	1.703	1.819	2.596
$L_2 \to H_{\sigma_0}^{1/2}$	0.284	0.333	0.101	1.846	1.445	1.763
$H_{\sigma_0}^{-1/2} \to L_2$	0.106	0.070	0.017	0.555	1.346	0.631

Table 4.5: Example 2 - Different angle: Localizations: The localization parameters also follow the same trend.

4.3.2 Discussion of example 2

The difference between this example and the reference example is the angle. We expect the same results for all values in the table. And indeed, the eigenvectors are now localized near $\frac{3\pi}{7}$ as opposed to $-\frac{\pi}{4}$ and all values are about the same. Some eigenvectors are flipped, but as explained in the second chapter, the Power Method may converge to the negative of the eigenvector with the biggest eigenvalue.

This example is a good indication for the proper workings of the algorithm, and it also shows that the $H_{\sigma_0}^{-1/2} \to H_{\sigma_0}^{1/2}$ convergence has no obvious relation to the angle of the inclusion.

Since the domain posesses circular symmetry and the execution of the algorithm seems to agree with that fact, this thesis will no longer be concerned with changing the angle of the inclusion. However, the domain is triangularized into areas that are assumed to have constant σ measures within, violating the symmetry slightly. The arising error will obviously depend on the angle of the inclusion, but it is the same error each time, suggesting that it is justified to neglect it.

Figure 4.3: Example 3 - Different distance from center: The optimal current patterns are more spread after changing the distance from the center from 0.6 to 0.1. They are close to being sinusoid.

(a) $L_2 \to L_2$ Robin

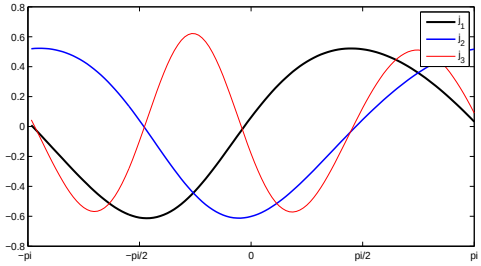

(b) $L_2 \to L_2$ Neumann

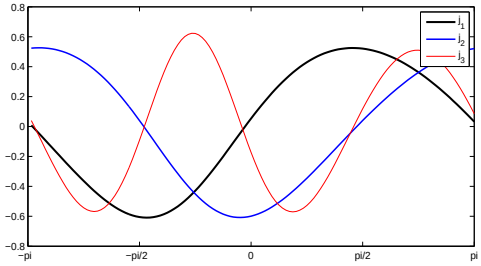

(c) $H_{\sigma_0}^{-1/2} \to H_{\sigma_0}^{1/2}$ Robin

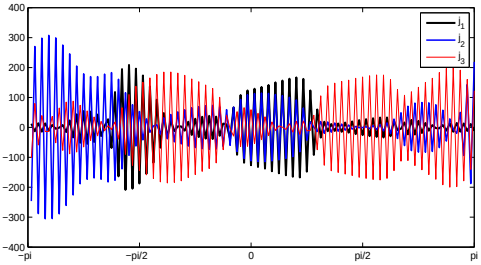

(d) $H_{\sigma_0}^{-1/2} \to H_{\sigma_0}^{1/2}$ Neumann

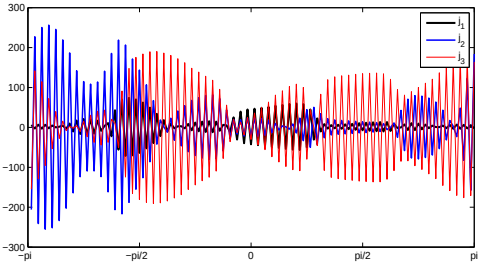

(e) $L_2 \to H_{\sigma_0}^{1/2}$ Robin

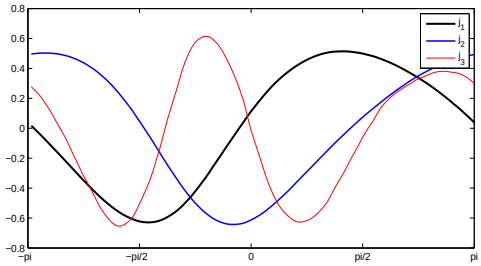

(f) $L_2 \to H_{\sigma_0}^{1/2}$ Neumann

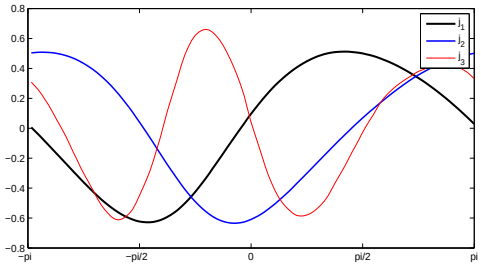

(g) $H_{\sigma_0}^{-1/2} \to L_2$ Robin

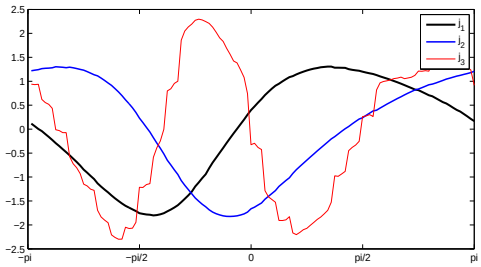

(h) $H_{\sigma_0}^{-1/2} \to L_2$ Neumann

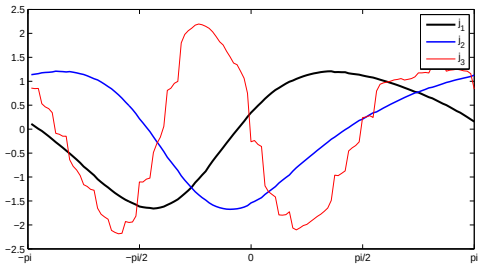

	λ_1	λ_2	λ_3
Robin-to-Dirichlet			
$L_2 \to L_2$	7.98e-005	7.69e-005	5.34e-008
$H_{\sigma_0}^{-1/2} \to H_{\sigma_0}^{1/2}$	9.93e-001	9.94e-001	9.93e-001
$L_2 \to H_{\sigma_0}^{1/2}$	5.26e-004	5.12e-004	2.74e-005
$H_{\sigma_0}^{-1/2} \to L_2$	5.28e-004	5.12e-004	1.89e-005
Neumann-to-Dirichlet			
$L_2 \to L_2$	1.52e-004	1.46e-004	7.63e-008
$H_{\sigma_0}^{-1/2} \to H_{\sigma_0}^{1/2}$	9.98e-001	9.92e-001	9.92e-001
$L_2 \to H_{\sigma_0}^{1/2}$	8.46e-004	8.23e-004	3.78e-005
$H_{\sigma_0}^{-1/2} \to L_2$	8.48e-004	8.22e-004	2.48e-005

Table 4.6: Example 3 - Different distance from center: Eigenvalues: The eigenvalues all worsen by about one order of magnitude, the ranking still holds.

	$Err(\bar{\theta}_1)$	$Err(\bar{\theta}_2)$	$Err(\bar{\theta}_3)$	$var_1(\theta)$	$var_2(\theta)$	$var_3(\theta)$
Robin-to-Dirichlet						
$L_2 \to L_2$	0.314	0.328	0.002	2.928	2.872	3.196
$H_{\sigma_0}^{-1/2} \to H_{\sigma_0}^{1/2}$	0.275	0.875	0.028	1.707	1.965	3.897
$L_2 \to H_{\sigma_0}^{1/2}$	0.325	0.327	0.040	2.845	2.788	2.779
$H_{\sigma_0}^{-1/2} \to L_2$	0.298	0.323	0.003	2.700	2.628	2.823
Neumann-to-Dirichlet						
$L_2 \to L_2$	0.315	0.328	0.003	2.946	2.885	3.190
$H_{\sigma_0}^{-1/2} \to H_{\sigma_0}^{1/2}$	0.267	1.037	0.039	1.717	1.560	3.493
$L_2 \to H_{\sigma_0}^{1/2}$	0.313	0.327	0.072	2.855	2.818	2.905
$H_{\sigma_0}^{-1/2} \to L_2$	0.299	0.324	0.000	2.718	2.637	2.837

Table 4.7: Example 3 - Different distance from center: Localizations: All spaces have very similar localization parameters. The variance is very high.

4.3.3 Discussion of example 3

This example changes the distance of the inclusion from the center of the domain.

The method is visibly less able to localize the inclusion. All optimal currents are much wider spread and centered further away from the angle of the inclusion.

The theory agrees with this fact. If the inclusion was circular symmetric, the actual optimal currents are sin functions displaced by any angle. The optimal currents in this example are very close to being sin functions. However, the pictures show that the algorithm, even for this setting, is still able to find the actual angle of the inclusion.

Besides the obvious increase in variance, the eigenvalues of all cases are significantly worse. But all spaces suffer equally, so this environmental change of the problem has the same effect on all space choices.

The pictures are also suggesting that the first two optimal currents are mirrored versions of each other, flipped at the angle of the inclusion. And indeed, they share eigenvalue, $Err(\bar{\theta})$ and $var(\theta)$. All space settings are suggesting that the optimal currents are in fact not localized at the angle of the inclusion, but rather about 0.3 away from it in either of the two directions.

Figure 4.4: Example 4 - Bigger radius of the inclusion: For a radius of the inclusion of 0.3 instead of 0.2, the shape of the currents change their pattern to having two peaks, each near the angle at which the inclusion begins or ends. All rankings stay the same.

(a) $L_2 \to L_2$ Robin

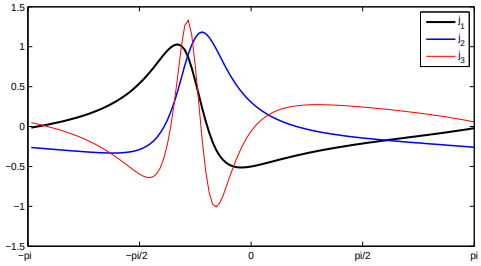

(b) $L_2 \to L_2$ Neumann

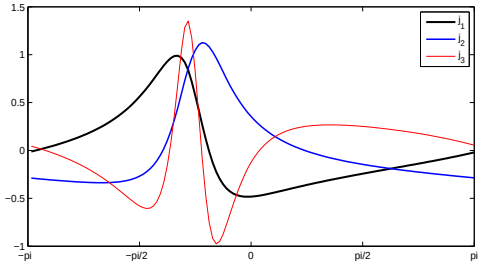

(c) $H^{-1/2}_{\sigma_0} \to H^{1/2}_{\sigma_0}$ Robin

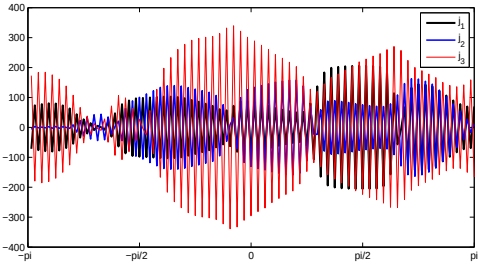

(d) $H^{-1/2}_{\sigma_0} \to H^{1/2}_{\sigma_0}$ Neumann

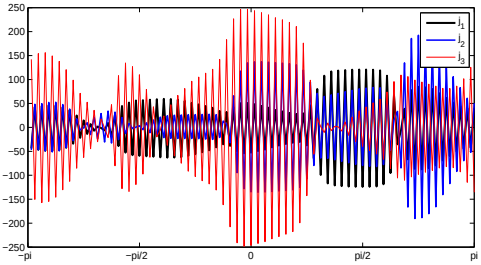

(e) $L_2 \to H^{1/2}_{\sigma_0}$ Robin

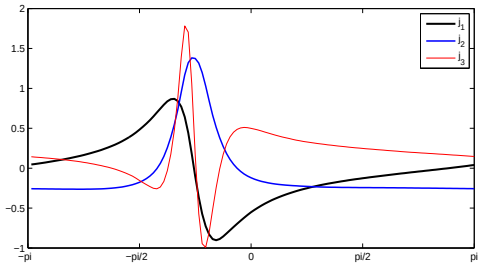

(f) $L_2 \to H^{1/2}_{\sigma_0}$ Neumann

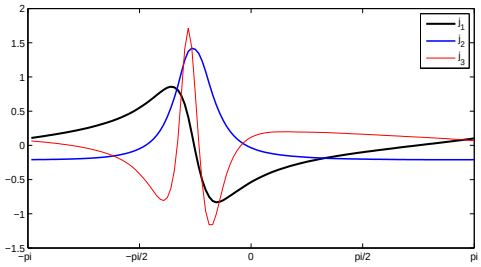

(g) $H^{-1/2}_{\sigma_0} \to L_2$ Robin

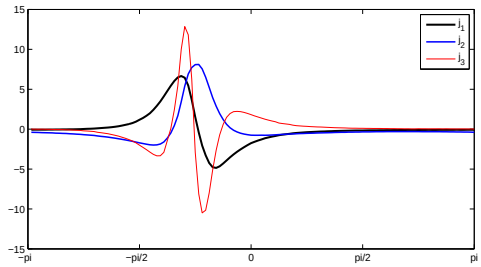

(h) $H^{-1/2}_{\sigma_0} \to L_2$ Neumann

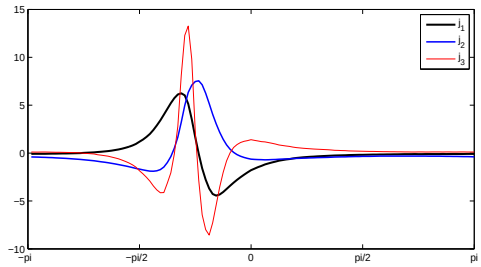

	λ_1	λ_2	λ_3
Robin-to-Dirichlet			
$L_2 \to L_2$	9.91e-004	9.63e-004	3.01e-005
$H_{\sigma_0}^{-1/2} \to H_{\sigma_0}^{1/2}$	9.98e-001	9.99e-001	9.90e-001
$L_2 \to H_{\sigma_0}^{1/2}$	1.14e-002	1.09e-002	1.24e-003
$H_{\sigma_0}^{-1/2} \to L_2$	1.15e-002	1.11e-002	1.32e-003
Neumann-to-Dirichlet			
$L_2 \to L_2$	1.52e-003	1.48e-003	3.84e-005
$H_{\sigma_0}^{-1/2} \to H_{\sigma_0}^{1/2}$	9.96e-001	1.00e+000	9.92e-001
$L_2 \to H_{\sigma_0}^{1/2}$	1.47e-002	1.40e-002	1.62e-003
$H_{\sigma_0}^{-1/2} \to L_2$	1.48e-002	1.43e-002	1.67e-003

Table 4.8: Example 4 - Bigger radius of the inclusion: Eigenvalues: The eigenvalues each increase by about one order of magnitude.

	$Err(\bar{\theta}_1)$	$Err(\bar{\theta}_2)$	$Err(\bar{\theta}_3)$	$var_1(\theta)$	$var_2(\theta)$	$var_3(\theta)$
Robin-to-Dirichlet						
$L_2 \to L_2$	0.291	0.260	0.204	1.588	2.107	1.883
$H_{\sigma_0}^{-1/2} \to H_{\sigma_0}^{1/2}$	0.415	0.352	0.364	3.542	2.912	2.960
$L_2 \to H_{\sigma_0}^{1/2}$	0.211	0.048	0.399	1.181	2.668	2.050
$H_{\sigma_0}^{-1/2} \to L_2$	0.136	0.084	0.043	0.576	1.252	0.439
Neumann-to-Dirichlet						
$L_2 \to L_2$	0.302	0.273	0.194	1.714	2.184	1.922
$H_{\sigma_0}^{-1/2} \to H_{\sigma_0}^{1/2}$	0.417	0.193	0.004	3.543	4.316	2.807
$L_2 \to H_{\sigma_0}^{1/2}$	0.017	0.028	0.173	1.269	2.394	1.561
$H_{\sigma_0}^{-1/2} \to L_2$	0.144	0.092	0.062	0.624	1.287	0.597

Table 4.9: Example 4 - Biger radius of the inclusion: Localizations: The localization parameters increase in accordance with the easier distinguishability for a bigger inclusion.

4.3.4 Discussion of example 4

This example changes the radius of the inclusion from 0.2 to 0.3. We expect that the optimal currents have a better ability to find the inclusion.

Indeed, the eigenvalues grow by $0.5 - 1$ orders of magnitude and the variance and sharpness of the optimal eigenvectors show a improving behavior. This is particularly visible in the $H_{\sigma_0}^{-1/2} \to L_2$ settings.

Again, the relation between the Neumann-to-Dirichlet problem and the Robin-to-Dirichlet problem is not affected, therefore the effect of a changing radius of the inclusion has equal influence on both settings.

However, this trend only holds if the inclusion is not too close to the boundary. If the boundary of the inclusion touches the boundary of the domain, the eigenvalues suddenly drop and the error and variance of the localization also stop giving meaningful information about σ_*. These effects will be further examined in the next section.

Another interesting feature of an environment with one big inclusion is the development of a second peak in the optimal current patterns. Each peak is then located near one of the angles at which the inclusion begins.

However, one peak is usually significantly bigger than the other one. This is not a violation of the symmetry of the problem because the second largest eigenvector has essentially the mirrored localization features and same eigenvalues.

Figure 4.5: Example 5 - Bigger peak: increasing the peak value of the inclusions has virtually no influence on the shape of the optimal current patterns

(a) $L_2 \to L_2$ Robin

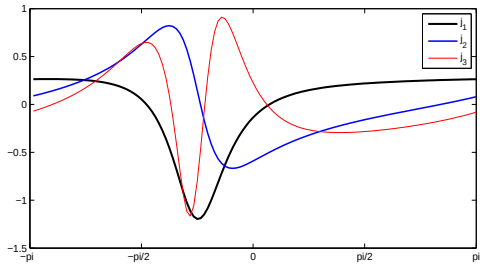

(b) $L_2 \to L_2$ Neumann

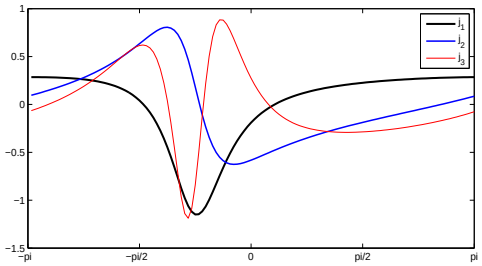

(c) $H_{\sigma_0}^{-1/2} \to H_{\sigma_0}^{1/2}$ Robin

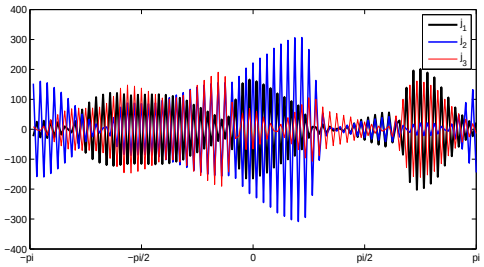

(d) $H_{\sigma_0}^{-1/2} \to H_{\sigma_0}^{1/2}$ Neumann

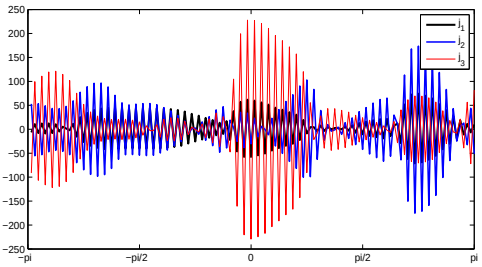

(e) $L_2 \to H_{\sigma_0}^{1/2}$ Robin

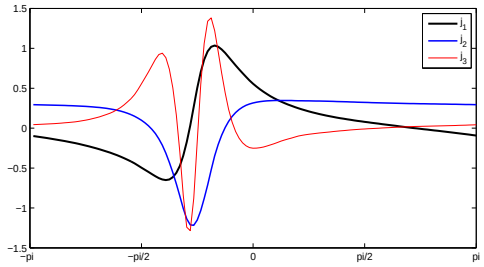

(f) $L_2 \to H_{\sigma_0}^{1/2}$ Neumann

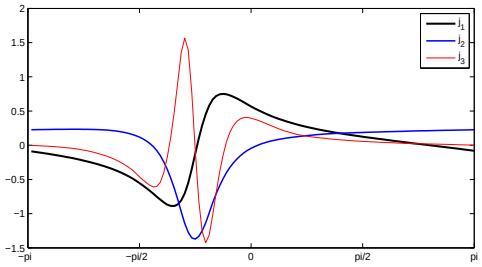

(g) $H_{\sigma_0}^{-1/2} \to L_2$ Robin

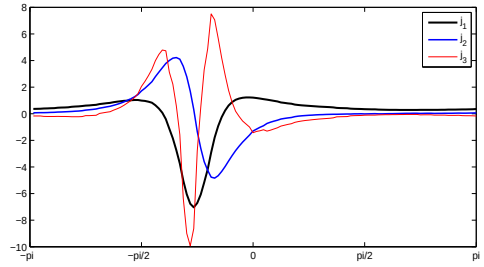

(h) $H_{\sigma_0}^{-1/2} \to L_2$ Neumann

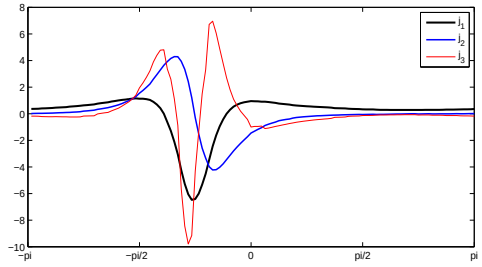

	λ_1	λ_2	λ_3
Robin-to-Dirichlet			
$L_2 \to L_2$	2.62e-004	2.51e-004	1.36e-006
$H_{\sigma_0}^{-1/2} \to H_{\sigma_0}^{1/2}$	9.90e-001	9.96e-001	9.91e-001
$L_2 \to H_{\sigma_0}^{1/2}$	2.85e-003	2.81e-003	7.09e-004
$H_{\sigma_0}^{-1/2} \to L_2$	2.95e-003	2.88e-003	1.52e-004
Neumann-to-Dirichlet			
$L_2 \to L_2$	4.23e-004	4.06e-004	1.85e-006
$H_{\sigma_0}^{-1/2} \to H_{\sigma_0}^{1/2}$	1.00e+000	9.89e-001	9.97e-001
$L_2 \to H_{\sigma_0}^{1/2}$	3.85e-003	3.82e-003	4.43e-004
$H_{\sigma_0}^{-1/2} \to L_2$	3.99e-003	3.89e-003	2.40e-004

Table 4.10: Example 5: Eigenvalues - Bigger peak: Increasing the peak from 10 to 20 has almost no influence on the eigenvalues.

	$Err(\bar{\theta}_1)$	$Err(\bar{\theta}_2)$	$Err(\bar{\theta}_3)$	$var_1(\theta)$	$var_2(\theta)$	$var_3(\theta)$
Robin-to-Dirichlet						
$L_2 \to L_2$	0.106	0.139	0.194	2.507	1.471	2.097
$H_{\sigma_0}^{-1/2} \to H_{\sigma_0}^{1/2}$	0.194	0.162	0.193	3.123	1.966	2.798
$L_2 \to H_{\sigma_0}^{1/2}$	0.041	0.094	0.149	1.180	2.945	0.716
$H_{\sigma_0}^{-1/2} \to L_2$	0.010	0.041	0.015	1.351	0.460	0.631
Neumann-to-Dirichlet						
$L_2 \to L_2$	0.127	0.163	0.186	2.583	1.582	2.119
$H_{\sigma_0}^{-1/2} \to H_{\sigma_0}^{1/2}$	0.193	0.299	0.095	3.122	4.034	2.839
$L_2 \to H_{\sigma_0}^{1/2}$	0.106	0.119	0.120	1.299	2.342	0.803
$H_{\sigma_0}^{-1/2} \to L_2$	0.027	0.043	0.022	1.389	0.470	0.671

Table 4.11: Example 5: Localizations - Bigger peak: The localizations are practically the same.

4.3.5 Discussion of example 5

In this example the peak of σ_*'s inclusion is changed from 10 to 20. We expect a general improvment of all values.

The improvement of the eigenvalues is very small, the improvment of the localization is barely noticeable.

This example suggests that a change in the peak has a weak influence on the distinguishability's norm in this environment. The localization parameters seem to depend mainly on the geometry of the inclusion. This makes sense because the inclusion has a spatial expansion after all, so it would be counterintuitive if the variance dropped below particular values at otherwise reasonable parameters.

This is an indication for the fact that the chosen value for the peak is at an order of magnitude that is completely distinguishable from the homogenous background by each choice of spaces and that it is not necessary to change this parameter in order to compare the optimal currents of each choice of spaces.

Figure 4.6: Example 6 - Bigger α: increasing α from 1 to 10 has a positive influence on the sharpness of all Robin settings.

(a) $L_2 \to L_2$ Robin

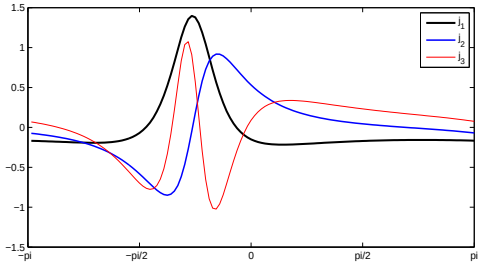

(b) $L_2 \to L_2$ Neumann

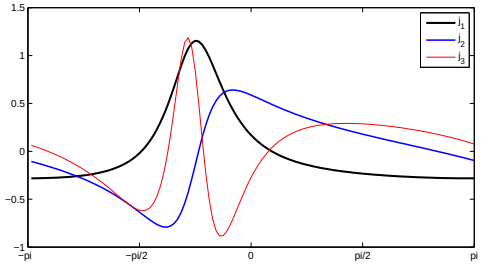

(c) $H_{\sigma_0}^{-1/2} \to H_{\sigma_0}^{1/2}$ Robin

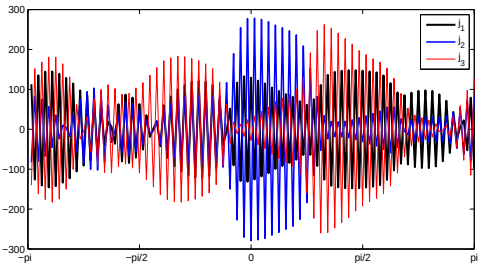

(d) $H_{\sigma_0}^{-1/2} \to H_{\sigma_0}^{1/2}$ Neumann

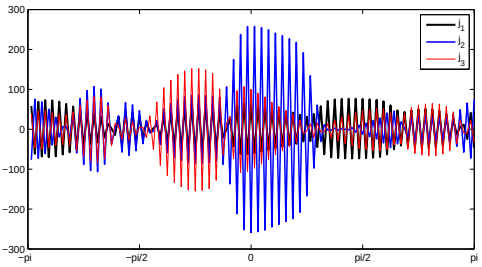

(e) $L_2 \to H_{\sigma_0}^{1/2}$ Robin

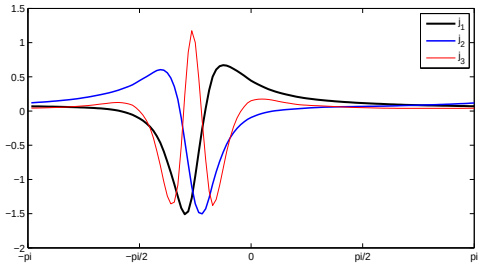

(f) $L_2 \to H_{\sigma_0}^{1/2}$ Neumann

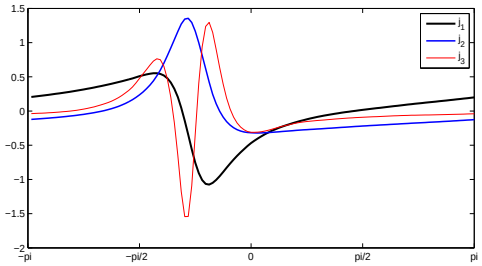

(g) $H_{\sigma_0}^{-1/2} \to L_2$ Robin

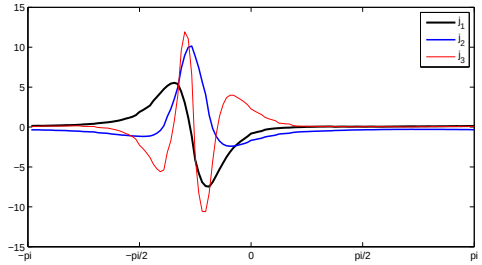

(h) $H_{\sigma_0}^{-1/2} \to L_2$ Neumann

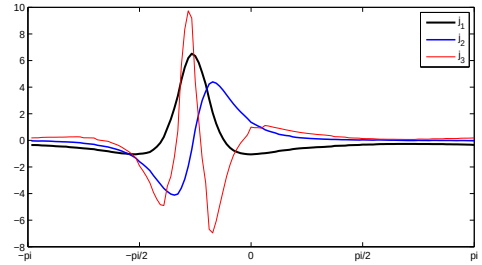

	λ_1	λ_2	λ_3
Robin-to-Dirichlet			
$L_2 \to L_2$	1.86e-005	1.78e-005	1.80e-007
$H_{\sigma_0}^{-1/2} \to H_{\sigma_0}^{1/2}$	9.94e-001	9.94e-001	9.93e-001
$L_2 \to H_{\sigma_0}^{1/2}$	4.99e-004	4.75e-004	1.29e-004
$H_{\sigma_0}^{-1/2} \to L_2$	4.95e-004	5.08e-004	5.68e-005
Neumann-to-Dirichlet			
$L_2 \to L_2$	3.54e-004	3.42e-004	1.51e-006
$H_{\sigma_0}^{-1/2} \to H_{\sigma_0}^{1/2}$	1.01e+000	9.93e-001	9.83e-001
$L_2 \to H_{\sigma_0}^{1/2}$	3.28e-003	3.20e-003	4.42e-004
$H_{\sigma_0}^{-1/2} \to L_2$	3.36e-003	3.31e-003	2.26e-004

Table 4.12: Example 6 - Bigger α: Eigenvalues: The eigenvalues of all Robin spaces drop by about one order of magnitude after changing α from 1 to 10.

	$Err(\bar{\theta}_1)$	$Err(\bar{\theta}_2)$	$Err(\bar{\theta}_3)$	$var_1(\theta)$	$var_2(\theta)$	$var_3(\theta)$
Robin-to-Dirichlet						
$L_2 \to L_2$	0.021	0.044	0.225	2.065	0.994	1.831
$H_{\sigma_0}^{-1/2} \to H_{\sigma_0}^{1/2}$	0.232	0.347	0.386	3.389	1.953	2.888
$L_2 \to H_{\sigma_0}^{1/2}$	0.267	0.263	0.025	1.288	1.272	0.891
$H_{\sigma_0}^{-1/2} \to L_2$	0.101	0.046	0.017	0.465	1.123	0.357
Neumann-to-Dirichlet						
$L_2 \to L_2$	0.107	0.141	0.187	2.607	1.574	2.118
$H_{\sigma_0}^{-1/2} \to H_{\sigma_0}^{1/2}$	0.236	0.252	0.049	3.398	1.920	2.548
$L_2 \to H_{\sigma_0}^{1/2}$	0.278	0.259	0.133	1.483	1.962	1.093
$H_{\sigma_0}^{-1/2} \to L_2$	0.006	0.000	0.019	1.374	0.450	0.663

Table 4.13: Example 6 - Bigger α: Localizations: The variance of the Robin settings improve significantly.

4.3.6 Discussion of example 6

This is probably the most interesting deviation from the reference example. In this example the parameter α of the Robin problem's boundary condition is changed from 1 to 10.

The Neumann problem does not use this parameter, so these results obviously stay the same, indicating that the algorithm is implemented properly.

For the Robin-to-Dirichlet simulations the eigenvalues greatly worsen, but $Err(\bar{\theta})$ and $var(\theta)$ experience a noticeable improvment. The shape of the eigenvectors agree with these values; they appear to be sharper and more localized near the angle of the inclusion. Because of these two-sided dynamics of the change of α, it is hard to decide whether or not the Robin problem is a better choice than the Neumann problem since it has to be decided if bigger eigenvalues or sharper localizations are desired.

The next section will point out more details about the dynamics of changing α.

Figure 4.7: Example 7 - Smaller background value: The effects are similar to the effects of the previous example.

(a) $L_2 \to L_2$ Robin

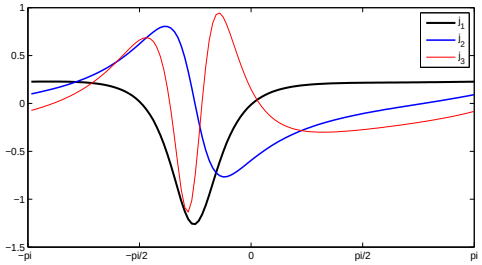

(b) $L_2 \to L_2$ Neumann

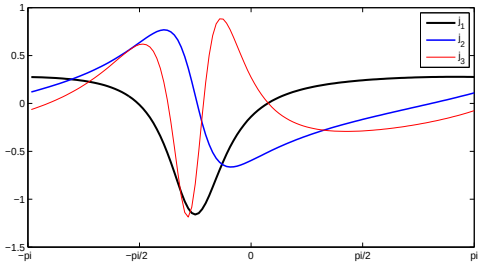

(c) $H_{\sigma_0}^{-1/2} \to H_{\sigma_0}^{1/2}$ Robin

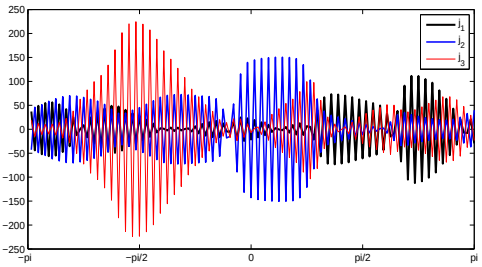

(d) $H_{\sigma_0}^{-1/2} \to H_{\sigma_0}^{1/2}$ Neumann

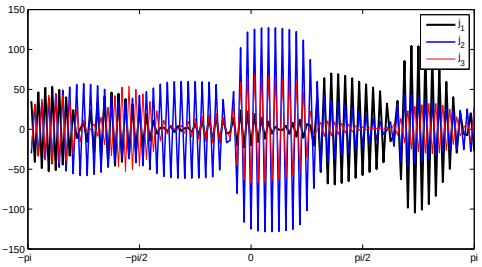

(e) $L_2 \to H_{\sigma_0}^{1/2}$ Robin

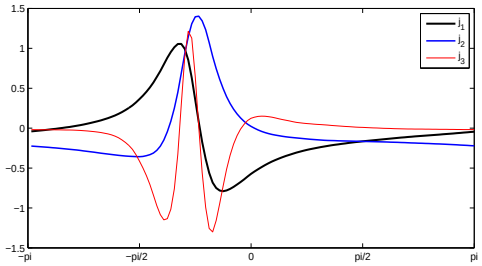

(f) $L_2 \to H_{\sigma_0}^{1/2}$ Neumann

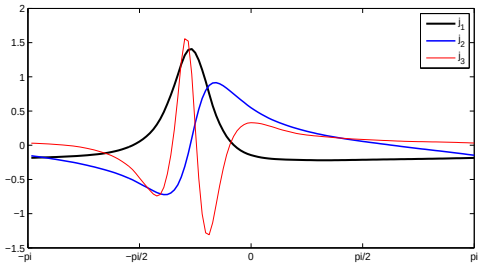

(g) $H_{\sigma_0}^{-1/2} \to L_2$ Robin

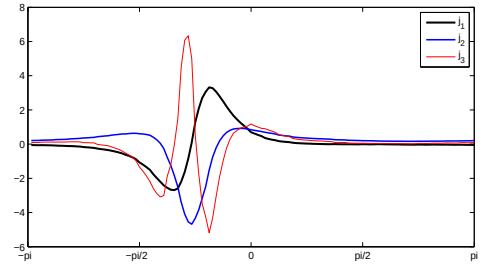

(h) $H_{\sigma_0}^{-1/2} \to L_2$ Neumann

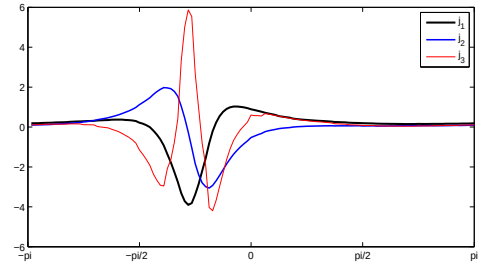

	λ_1	λ_2	λ_3
Robin-to-Dirichlet			
$L_2 \to L_2$	8.40e-004	8.08e-004	5.27e-006
$H_{\sigma_0}^{-1/2} \to H_{\sigma_0}^{1/2}$	9.96e-001	1.00e+000	9.90e-001
$L_2 \to H_{\sigma_0}^{1/2}$	4.32e-003	4.21e-003	1.01e-003
$H_{\sigma_0}^{-1/2} \to L_2$	4.37e-003	4.43e-003	3.14e-004
Neumann-to-Dirichlet			
$L_2 \to L_2$	2.68e-003	2.59e-003	1.14e-005
$H_{\sigma_0}^{-1/2} \to H_{\sigma_0}^{1/2}$	9.96e-001	1.00e+000	9.92e-001
$L_2 \to H_{\sigma_0}^{1/2}$	8.77e-003	9.04e-003	1.19e-003
$H_{\sigma_0}^{-1/2} \to L_2$	9.18e-003	9.16e-003	6.22e-004

Table 4.14: Example 7 - Smaller background value: Eigenvalues: All eigenvalues are increasing after decreasing σ_0. Due to a resulting bigger influence of α, the increase of the Neumann eigenvalues is stronger

	$Err(\bar{\theta}_1)$	$Err(\bar{\theta}_2)$	$Err(\bar{\theta}_3)$	$var_1(\theta)$	$var_2(\theta)$	$var_3(\theta)$
Robin-to-Dirichlet						
$L_2 \to L_2$	0.031	0.042	0.205	2.415	1.309	2.045
$H_{\sigma_0}^{-1/2} \to H_{\sigma_0}^{1/2}$	0.036	0.147	0.342	5.079	2.096	2.124
$L_2 \to H_{\sigma_0}^{1/2}$	0.356	0.216	0.076	1.312	2.159	0.496
$H_{\sigma_0}^{-1/2} \to L_2$	0.070	0.025	0.009	0.454	1.273	0.551
Neumann-to-Dirichlet						
$L_2 \to L_2$	0.077	0.104	0.187	2.635	1.563	2.118
$H_{\sigma_0}^{-1/2} \to H_{\sigma_0}^{1/2}$	0.023	0.195	0.218	5.066	2.304	2.550
$L_2 \to H_{\sigma_0}^{1/2}$	0.081	0.131	0.134	2.316	1.330	1.034
$H_{\sigma_0}^{-1/2} \to L_2$	0.089	0.133	0.019	1.275	0.693	0.663

Table 4.15: Example 7 - Smaller background value: Localizations: The localization features of the Neumann settings do not change, the values of the Robin settings are slightly improved.

4.3.7 Discussion of example 7

For this example the homogenous background changes from 5.5 to 2. Note that the peak is scaled accordingly in a way that the quotient between peak and background stays the same.

The development of the values suggests that the Robin and Neumann problems perform better, but the increased influence of α in the PDE causes the Robin eigenvalues to drop marginally in accordance with the previous example, the localization parameters also show similar behavior. Therefore this change of the background value has the same influence as a larger influence of the Dirichlet term in the Robin problem and a general scaling of all eigenvalues.

What happened here is that σ was decreased without adjusting α, which essentially puts more emphasis on the Dirichlet term of the problem and scales the problem.

There are no new dynamics to be examined for a changing background conductivity, it merely involves adjusted scaling. Because of this it is not discussed in more detail for the rest of the thesis.

Figure 4.8: Example 8 - Increased accuracy: The current patterns have the same shape as the reference example

(a) $L_2 \to L_2$ Robin

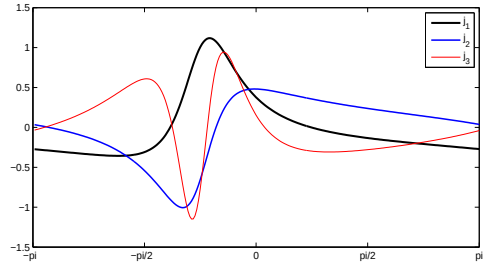

(b) $L_2 \to L_2$ Neumann

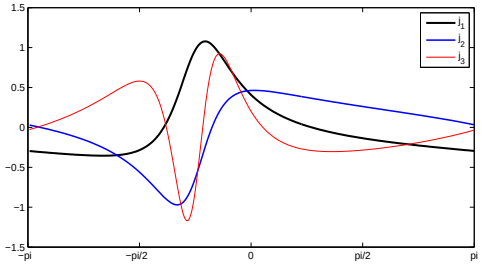

(c) $H_{\sigma_0}^{-1/2} \to H_{\sigma_0}^{1/2}$ Robin

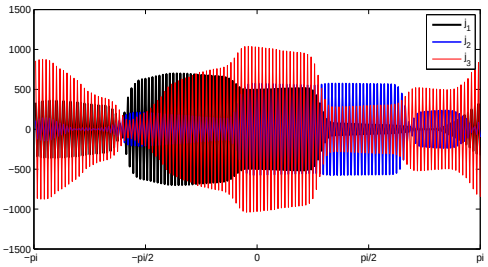

(d) $H_{\sigma_0}^{-1/2} \to H_{\sigma_0}^{1/2}$ Neumann

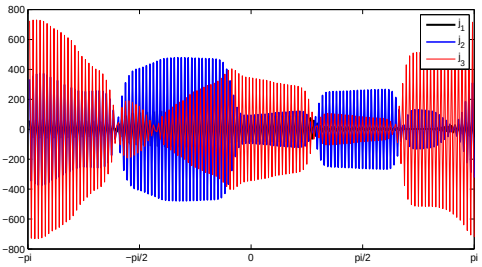

(e) $L_2 \to H_{\sigma_0}^{1/2}$ Robin

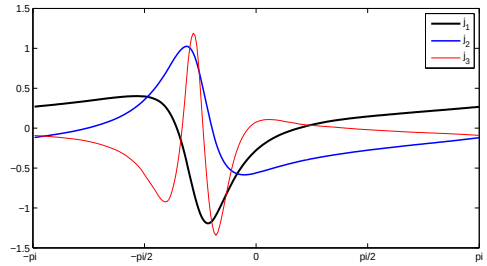

(f) $L_2 \to H_{\sigma_0}^{1/2}$ Neumann

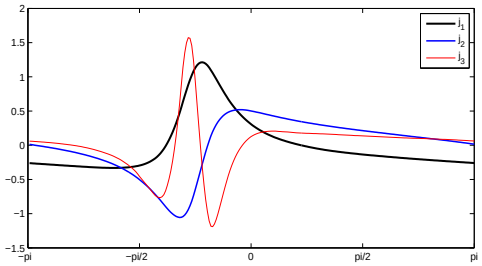

(g) $H_{\sigma_0}^{-1/2} \to L_2$ Robin

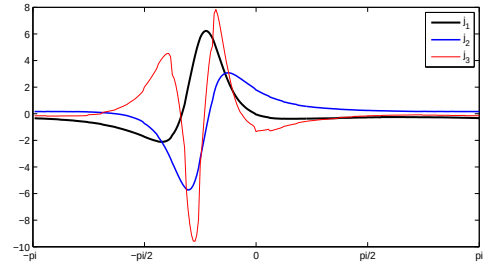

(h) $H_{\sigma_0}^{-1/2} \to L_2$ Neumann

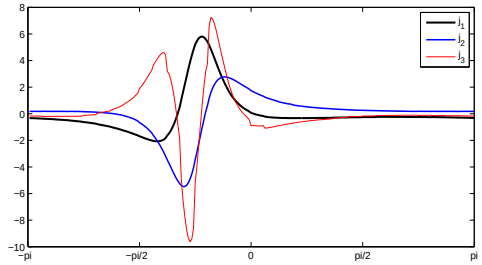

	λ_1	λ_2	λ_3
Robin-to-Dirichlet			
$L_2 \to L_2$	2.05e-004	2.01e-004	8.48e-007
$H_{\sigma_0}^{-1/2} \to H_{\sigma_0}^{1/2}$	1.00e+000	1.00e+000	9.99e-001
$L_2 \to H_{\sigma_0}^{1/2}$	2.19e-003	2.17e-003	3.79e-004
$H_{\sigma_0}^{-1/2} \to L_2$	2.24e-003	2.20e-003	7.44e-005
Neumann-to-Dirichlet			
$L_2 \to L_2$	3.33e-004	3.25e-004	1.13e-006
$H_{\sigma_0}^{-1/2} \to H_{\sigma_0}^{1/2}$	1.00e+000	1.00e+000	9.99e-001
$L_2 \to H_{\sigma_0}^{1/2}$	3.00e-003	2.98e-003	2.48e-004
$H_{\sigma_0}^{-1/2} \to L_2$	3.07e-003	3.01e-003	1.42e-004

Table 4.16: Example 8: Eigenvalues - Increased accuracy: The eigenvalues agree with the reference example.

	$Err(\bar{\theta}_1)$	$Err(\bar{\theta}_2)$	$Err(\bar{\theta}_3)$	$var_1(\theta)$	$var_2(\theta)$	$var_3(\theta)$
Robin-to-Dirichlet						
$L_2 \to L_2$	0.279	0.303	0.214	2.091	1.705	2.000
$H_{\sigma_0}^{-1/2} \to H_{\sigma_0}^{1/2}$	0.152	0.924	0.054	1.510	1.939	2.905
$L_2 \to H_{\sigma_0}^{1/2}$	0.314	0.407	0.340	2.087	1.906	0.910
$H_{\sigma_0}^{-1/2} \to L_2$	0.148	0.180	0.037	1.204	0.874	0.676
Neumann-to-Dirichlet						
$L_2 \to L_2$	0.287	0.309	0.208	2.174	1.800	2.024
$H_{\sigma_0}^{-1/2} \to H_{\sigma_0}^{1/2}$	0.152	0.110	0.783	1.515	2.519	2.717
$L_2 \to H_{\sigma_0}^{1/2}$	0.277	0.298	0.140	2.079	1.559	1.416
$H_{\sigma_0}^{-1/2} \to L_2$	0.158	0.183	0.038	1.189	0.934	0.721

Table 4.17: Example 8: Localizations - Increased accuracy: The localization parameters are slightly different due to the different discretization.

4.3.8 Example 8

This example shows that a finer mesh and an increased number of Power Method iterations do not change the results for $\lambda, Err(\theta)$ and $var(\theta)$.

However, a finer mesh makes the inclusion of σ_* closer to being circular, thus changing the geometry of the problem slightly.

4.4 Results of the simulation

This section will show the dependence of $\lambda, Err(\theta), var(\theta)$ of various parameters. The parameters for the following set of experiments are all fixed except for one parameter. The standard setting is as follows:

The guess σ_0 is constant over the domain with value $\sigma_0 = 5.5$. σ_* has σ_0 as background with an additional circular peak with a value of 9 times the background value and a radius of 0.3 located at an angle of $-\frac{3}{7}\pi$ with a distance of 0.6 from the center of the domain.

The domain is circular with radius 1 and the parameter $\alpha = 1$.

Each experiment consists of 30 optimizations equally distributed over the range that the changing parameter is chosen in, each with 250 iterations.

The $H_{\sigma_0}^{-1/2} \rightarrow H_{\sigma_0}^{1/2}$ spaces are left out because they are not a reasonable choice and would confuse the reader. The three remaining space combinations and the respective Neumann results are compared with respect to $\lambda, Err(\theta)$ and $var(\theta)$.

4.4.1 Changing the position of the inclusion

For this experiment, the single changing parameter is the position of the peak of σ_*. It is chosen to be between 0 and 1.

Figure 4.9 shows that the eigenvalues of each space increase exponentially while the distance of the inclusion from the center increases until the inclusion intersects with the boundary of the domain. This trend is similar for all spaces; it is so similar that the quotient

between the eigenvalues seems to be constant over the whole data set for any choice of two spaces. This result agrees with recent studies.

In general, the eigenvalues of the Neumann spaces are better, but it appears as if a slight global constant scaling of the Neumann eigenvalues will lead to the exact Robin results. The best spaces are $H_{\sigma_0}^{-1/2} \to L_2$, followed by $L_2 \to H_{\sigma_0}^{1/2}$

$Err(\theta)$ does not seem to follow an obvious trend, but some observations are possible: If the distance is below 0.18, all spaces have difficulties localizing the inclusion. If the distance increases above 0.8, all errors decrease significantly, which unfortunately is not part of a reasonable distance choice. For any fixed data point $L_2 \to H_{\sigma_0}^{1/2}$ mostly has the worst performance, but no proper statements can be made.

The variance gives a better insight. It is very noisy due to the huge uncertainty of $Err(\theta)$, but it is apparent that the variance of $H_{\sigma_0}^{-1/2} \to L_2$ drops faster than the variance of $L_2 \to L_2$ as the distance increases. $L_2 \to H_{\sigma_0}^{1/2}$ is mostly between those two. The performance of the Neumann spaces is almost always worse, so even though the Robin spaces have smaller eigenvalues, they are sharper and more localized near the inclusion.

Figure 4.9: Changing the position of the inclusion: As the distance from the center increases, the eigenvalues grow exponentially and the variance decreases. $Err(\theta)$ is hard to predict.

(a) λ_1

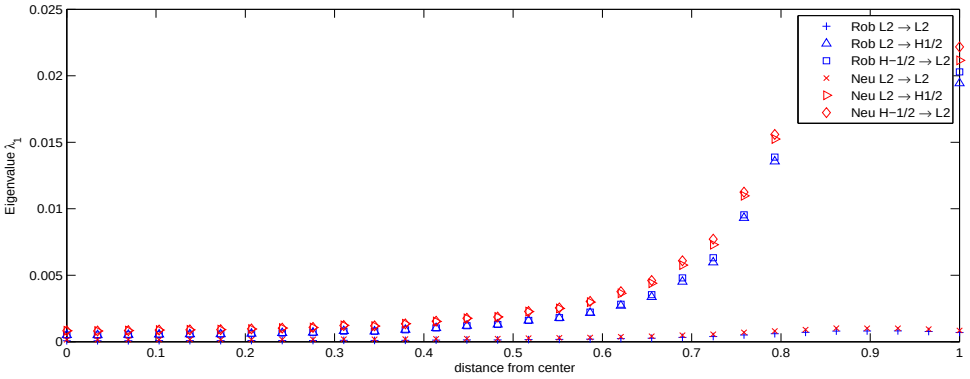

(b) $Err(\theta_1)$

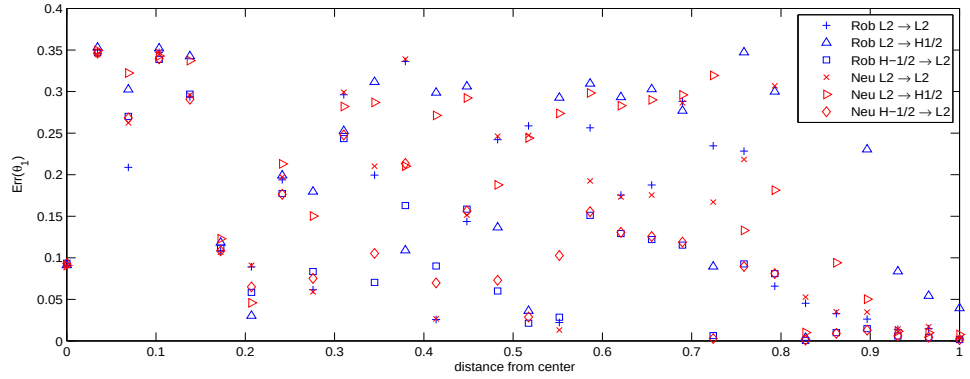

(c) $var(\theta_1)$

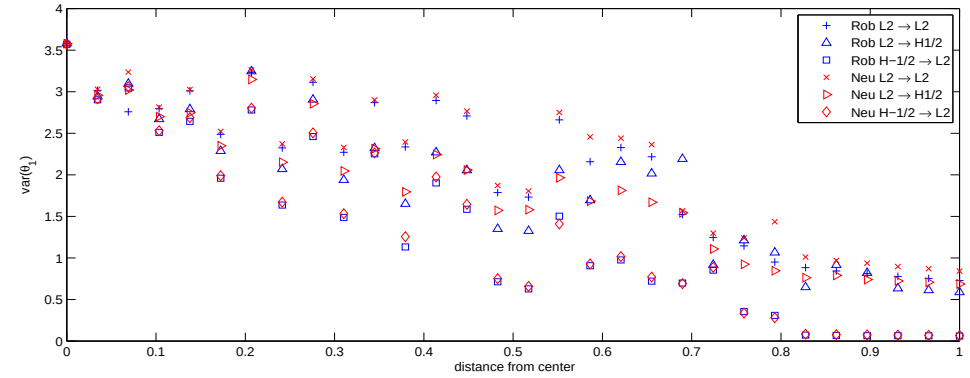

4.4.2 Changing size of the inclusion

Here, the properties of the optimal currents with a size of the peak between 0 and 0.7 are discussed, the inclusion is now centered at a distance of 0.4 from the center of the domain.

Figure 4.10 shows that the eigenvalues seem to grow exponentially as the size of the inclusion increases; this is also in agreement with recent studies. The ranking of the spaces is the same as in the previous examples.

The error in angle and the variance do not allow any strong statements about the performance of the proposed spaces, but it appears as if the variance of $H_{\sigma_0}^{-1/2} \to L_2$ is often best, the variance of $L_2 \to H_{\sigma_0}^{1/2}$ is worst most of the times and $L_2 \to H_{\sigma_0}^{1/2}$ somewhere in between those two. The performance of the Robin environments is slightly better in almost all cases.

Figure 4.10: Changing the size of the inclusion: As the size of the inclusion increases, the eigenvalues seem to grow exponentially. $Err(\theta)$ and $var(\theta)$ are hard to predict.

(a) λ_1

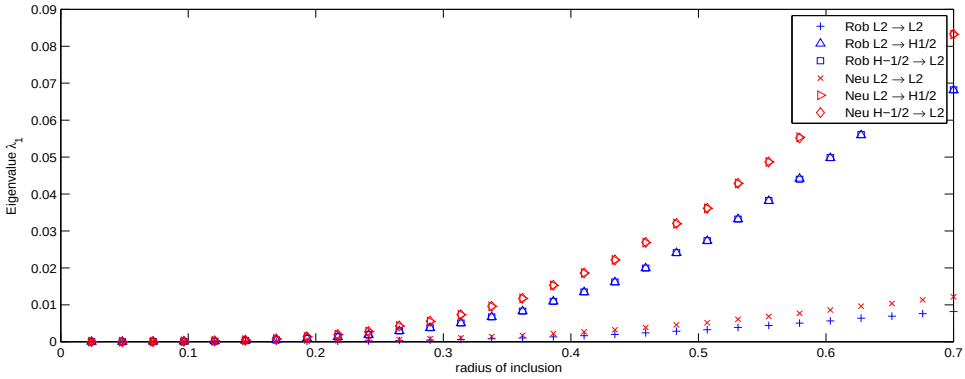

(b) $Err(\theta_1)$

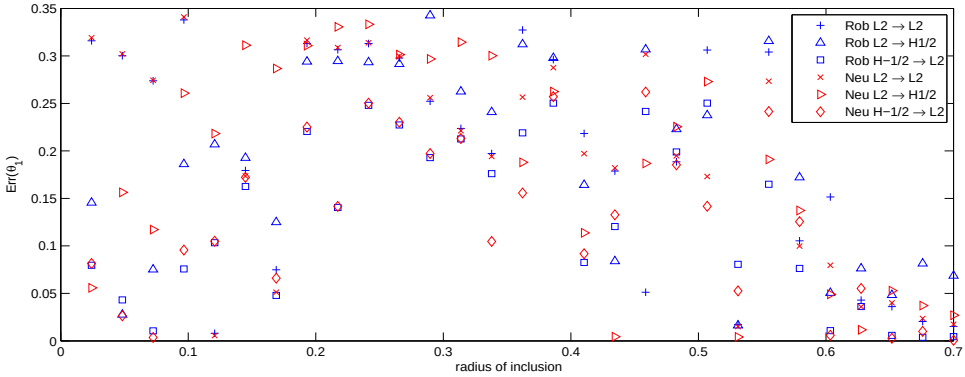

(c) $var(\theta_1)$

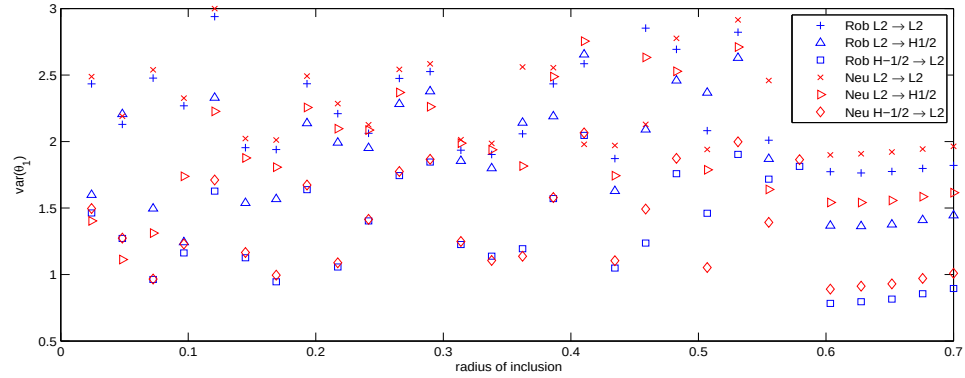

4.4.3 Changing intensity of the inclusion

In this experiment we examine the change in the optimal currents for a height of the peak between 0 and 15 times the background value. Figure 4.11 shows the results.

This time, the behavior of the eigenvalue is a concave function, meaning that for any choice of spaces and given a reasonable contrast it is possible to distinguish between the guess and the physical data, and each equal increase in contrast has less influence on the results than the previous one.

$Err(\theta)$ and $var(\theta)$ are more or less constant over the whole experiment after a contrast factor of about 5, meaning that a higher factor does not affect the geometry of the optimal currents.

Figure 4.11: Changing the intensity of the inclusion: The increasing contrast has concave influence on the eigenvalues and stops affecting the localizatin quickly.

(a) λ_1

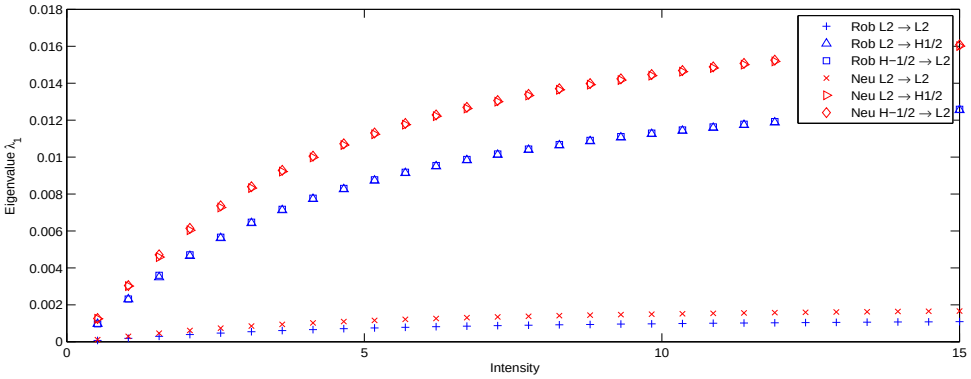

(b) $Err(\theta_1)$

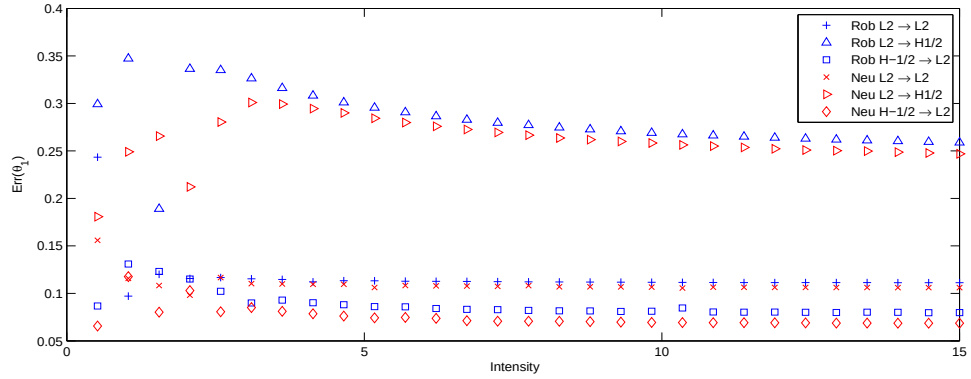

(c) $var(\theta_1)$

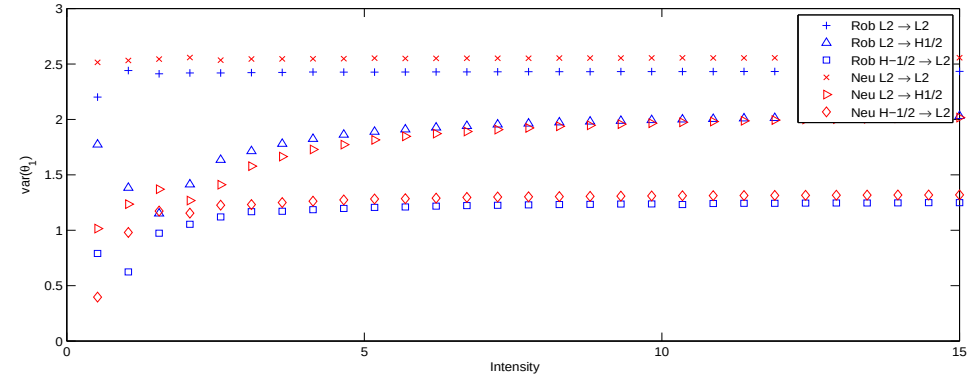

4.4.4 Changing parameter α

The impact of α being in the range between 0.001 and 15 is discussed in this experiment. Figure 4.12 shows the results.

This is probably the most interesting figure of this paper. The eigenvalues of all Neumann space settings are obviously constant because the parameter does not influence these calculations. The eigenvalues for the Robin spaces converge towards the corresponding Neumann values for $\alpha \to 0$ which is what we hoped for because the PDE converges in the same manner. As α increases, the eigenvalues experience an exponential-like decay with a half-life period of about 6. This fact makes them less preferable for applications because the consequent measurement errors would have a bigger influence.

However, the localization parameters get noticeably sharper, so it might be worth considering to choose the Robin setting after all. The variance seems to drop by up to half if α is chosen to be big enough and all $Err(\theta)$ values converge to one unique angle which is not the angle of the center of the inclusion. This suggests that there is one pair of optimal currents that is unique for all spaces if α is chosen to be big enough. Each of them being away from the angle of the inclusion by the same angle and are each very sharply localized.

Figure 4.12: Changing the Robin problem's parameter α: The Neumann problem is not affected at all, the eigenvalues of the Robin problems seem to decay exponentially as α increases, the variance is decreasing and $Err(\theta)$ seems to converge to a value that is shared by all spaces.

(a) λ_1

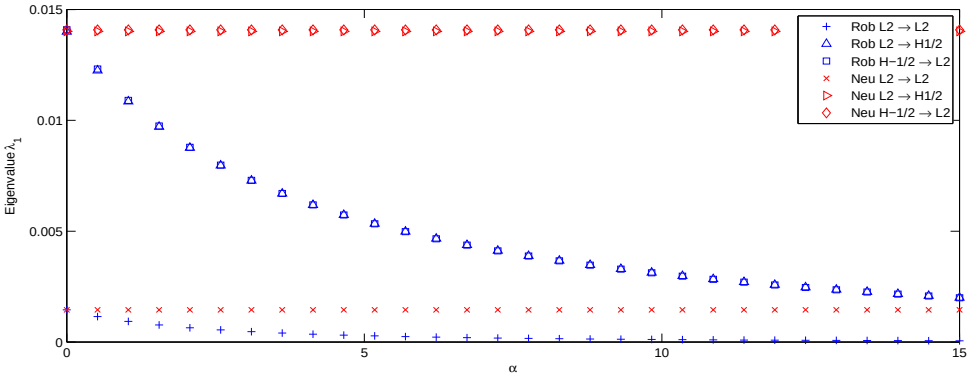

(b) $Err(\theta_1)$

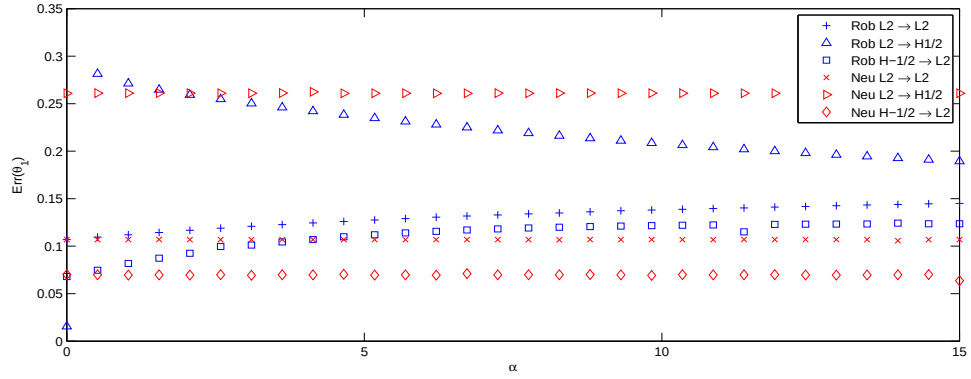

(c) $var(\theta_1)$

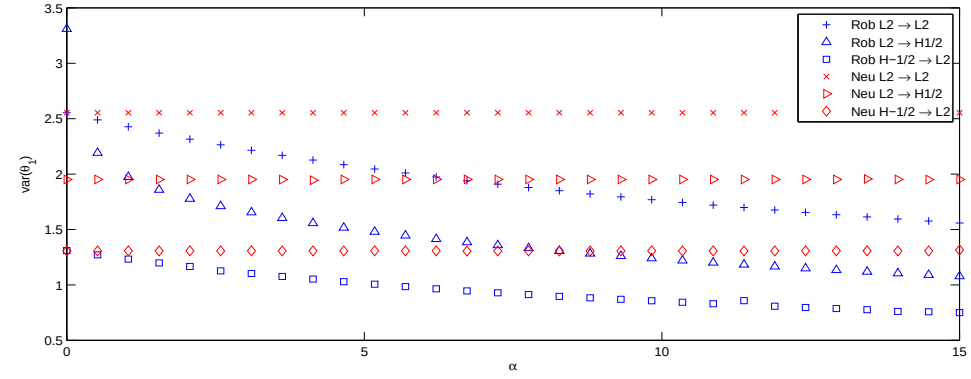

4.5 Limits of the simulation

The nature of the problem makes it practically impossible to distinguish between conductivities that differ solely near the center of the domain. Thus experiments with parameters that pose the problem in an environment close to being emphasized at the middle of the domain will be very prone to numerical errors and might - in case of circular symmetry for example - even converge with dependence of the initial data.

However if the inclusions are too close to the boundary or even cross the boundary, the approximations are violating assumptions that are made in the analytical part and should therefore be ignored due to a lack of knowledge about the dynamics of inclusions close to the boundary. For example, the identities described in (3.5)-(3.10) cease to hold.

Also the performance measure for the localization can not be used properly to make statements when the geometry of the inclusion changes. This is caused by the fact that the optimal currents seem to be localized near the center of the inclusion, but most definitely not at the center of the inclusion. Thus it is not reasonable to assume that $Err(\theta) = 0$ for a good optimal current. It is also possible that an optimal choice is a pair of symmetrically localized eigenvectors with the same eigenvalues.

The variance has similar issues: Since the inclusion has a spatial expansion, it is not reasonable to expect a variance that is very small.

However, the performance measures reflect the trend that is apparent from looking at the eigenvectors.

Chapter 5

Discussion of the results

5.1 Advantages and disadvantages of the Robin setting

Any Robin space setting generally performs worse regarding eigenvalues, but better regarding the localization factors when compared with the corresponding Neumann space setting. This trend is virtually never broken, stronger for a big α and vanishes as $\alpha \to 0$. A cross-comparison between the Robin and Neumann space choices is not necessary because the spaces share dynamics and rankings for either boundary condition among themselves: $L_2 \to L_2$ is always the smoothest with the smallest eigenvalue, $L_2 \to H^{1/2}_{\sigma_0}$ is always ranked second and $H^{-1/2}_{\sigma_0} \to L_2$ always has the biggest eigenvalues and sharpest localization.

Even though including the extra term in the boundary condition makes the model more physical, the smaller eigenvalues may cause problems because they result in the noise having more influence on the information that is extracted from the application, which might be a price that is too high for the sharper localization.

5.2 Future work

It is still not obvious how to decide which choice of spaces results in better performance of the optimal currents. The eigenvalues are definitely easy to analyze and important for a good optimal current, but the localization measures do not adequately reflect the ob-

servable properties of the optimal currents. A different localization measure or an improved version that is more involved with the spatial expansion of the inclusion is important and still an open question.

Using a distinguishability criterion that is involved with the solution of the PDE instead of the outcome of the measurement on the Dirichlet boundary results in four additional space choices each for the Robin- and Neumann problems. The theory stays the same and the adjoint calculations should follow a similar trend. They should even be easy to implement into the existing simulation.

Optical Tomography shares many problems with Electrical Impedance Tomography due to the very similar nature of the corresponding PDEs and the similarity in the image reconstruction algorithm. The basic idea of optimal sources are the same and the methods that are used are heavily related. The question of optimal sources is also still open and recent results have shown that replacing the Neumann boundary value problem with a Robin boundary value problem can improve the model error and image quality of Optical Tomography significantly.

Bibliography

[1] M. Cheney, D. Isaacson, and J. Newell. Electrical impedance tomography. 41(1):85–101, 1999.

[2] L. C. Evans. Partial differential equations. 19.

[3] B. Jacob, B. Jin, T. Khan, and P. Maass. Comparison of eight distinguishability criteria in optical imaging. 2011.

[4] B. Jin, T. Khan, P. Maass, and M. Pidcock. Function spaces and optimal currents in impedance tomography. *DFG-Schwerpunktprogramm 1324*, 2009.

[5] R. E. Schowalter. Hilbert space methods for partial differential equations. 1994.